

# Integrated Lasers with Transition-Metal-Dichalcogenide Heterostructures: Analysis and Design Utilizing Coupled-Mode Theory for Two-Dimensional Materials

Georgios Nousios<sup>1</sup>,<sup>1</sup> Thomas Christopoulos<sup>1,\*</sup>,<sup>1,\*</sup> Odysseas Tsilipakos<sup>2</sup>,<sup>2</sup> and Emmanouil E. Kriezis<sup>1</sup>

<sup>1</sup>*School of Electrical and Computer Engineering, Aristotle University of Thessaloniki (AUTH), Thessaloniki GR-54124, Greece*

<sup>2</sup>*Theoretical and Physical Chemistry Institute, National Hellenic Research Foundation, Athens GR-11635, Greece*

 (Received 28 September 2022; revised 3 April 2023; accepted 12 May 2023; published 8 June 2023)

We assess the continuous-wave and dynamic performance of a photonic laser cavity consisting of a silicon-rich-nitride-on-insulator disk resonator overlaid with a transition-metal dichalcogenide (TMD) bilayer heterostructure ( $\text{WSe}_2/\text{MoS}_2$ ) acting as the gain medium. The optically pumped TMD heterostructure fosters an interlayer exciton with long radiative recombination lifetime, providing light emission in the near-infrared ( $\sim 1130$  nm). Following a meticulous design process, we propose a silicon-on-insulator-compatible, monolithically integrated optical source capable of emitting milliwatt power inside an integrated waveguide, featuring a low pump-power threshold of  $\sim 16$  kW/cm<sup>2</sup>, and exhibiting an estimated total quantum efficiency of approximately 1.7%. The proposed laser cavity is analyzed and designed using a rigorous theoretical framework based on perturbation theory and temporal coupled-mode theory, capable of treating nanophotonic cavities of any geometry and material composition comprising both bulk and/or sheet gain media. The framework is built upon fundamental electromagnetic and semiclassical gain equations, rendering it general and adaptable to different cavity configurations and gain-media descriptions. It constitutes a powerful tool for the efficient analysis of contemporary micro- and nanophotonic semiconductor lasers, since it is capable of predicting fundamental laser characteristics, providing design directives, deriving continuous-wave design metrics, and evaluating the dynamic response of realistic laser cavities.

DOI: [10.1103/PhysRevApplied.19.064027](https://doi.org/10.1103/PhysRevApplied.19.064027)

## I. INTRODUCTION

Efficient and reliable on-chip light sources, compatible with the commercial silicon-on-insulator (SOI) platform, constitute a key prerequisite for today's optical industry. Yet, this goal is far from being achieved. Silicon, an indirect-band-gap semiconductor, is transparent in the near-infrared (NIR) and cannot be used as a direct light source in the communication O and C bands. Silicon photonics has thrived from the mid-2000s onwards for passive photonic circuitry, and hybrid integration with other semiconductors, such as germanium or III-V compounds, remains a promising approach towards integrated light sources [1,2]. This strategy, however, entails technological challenges when large-scale integration is considered, mostly due to material incompatibility (lattice mismatch).

More recently, other novel materials such as metal-halide perovskites have also been proposed for integration with silicon [2]; nevertheless, this solution is currently

immature and mostly used in light-emitting diodes (LEDs) [3]. In parallel, other CMOS-compatible platforms have been examined, such as the complementary-to-SOI platforms of silicon-nitride-on-insulator (SNOI) and silicon-rich-nitride-on-insulator (SRNOI) [4,5]. SNOI and SRNOI are very successful for passive photonic circuitry, since they share the same advantages as the SOI platform (dense integration, low voltage control, etc.), and in addition, due to the larger band gap of silicon nitride ( $\text{Si}_3\text{N}_4$ ), they also exhibit an expanded transparency window (up to the visible spectrum) and are not affected by nonlinear losses (two-photon absorption) and the accompanying free-carrier effects.

Two-dimensional (2D) materials have recently attracted increasing attention for active photonic and optoelectronic devices (modulators, photodetectors, and light sources), due to their unique absorption and emission properties, the strong light-matter interaction they can provide, as well as their compatibility with the SOI platform [6–9]. Graphene, black phosphorus, and hexagonal boron nitride have been considered as candidates for on-chip light emission.

\*Corresponding author. [cthomasa@ece.auth.gr](mailto:cthomasa@ece.auth.gr)

An even-more-promising family of 2D materials for integrated light sources can be transition-metal dichalcogenides (TMDs) and their heterostructures [2,6]. TMD monolayers are direct-band-gap semiconductors with special excitonic properties [10] that have been exploited in a number of lasing structures in the deep NIR [11] and visible regions [12,13]. Moreover, bilayer heterostructures formed by the vertical stacking of two different TMD monolayers lead to the formation of a type-II band alignment, hosting interlayer excitons with long radiative recombination lifetimes and an emission wavelength that depends on the individual monolayers. The emission wavelength of the TMD bilayer heterostructures can also be electrically tuned through the Stark effect [14–16], providing a valuable degree of freedom in practical optoelectronic devices. Therefore, TMD heterostructures constitute a promising 2D gain material family, and a number of works have been published recently aiming to investigate their unique luminescence properties [14–21] and demonstrate their inclusion in novel photonic laser structures emitting in the NIR [22,23]. Currently, the incorporation of TMD bilayers in micro- and nanocavity configurations is deemed a promising route towards practical, integrated light-emitting sources characterized by compact size, power efficiency, and high modulation speed [24].

Motivated by the aforementioned developments, in this work we theoretically study and design a practical laser cavity consisting of an SRNOI [25–28] disk resonator which supports tightly confined, whispering-gallery modes. The gain is provided by a MoS<sub>2</sub>/WSe<sub>2</sub> bilayer residing on top of the cavity, where it interacts strongly with the supported mode and allows for efficient optical pumping from above. The proposed laser structure is optically pumped at 740 nm and emits light at 1128 nm. To accurately evaluate the overall response of the laser under study, we develop a rigorous framework based on temporal coupled-mode theory (CMT) [29]. CMT provides an accurate and computationally efficient approach to assess the response of linear [30,31] and nonlinear resonators [32,33], supporting a broad range of single- or multichannel nonlinear phenomena [34].

The framework to be presented is general and can be exploited for both bulk and sheet-type gain materials, expanding previously reported works [35]. In addition, it can be utilized to assess both the continuous-wave (CW) characteristics (lasing threshold, lasing frequency, and emitted power), as well as the temporal response of the laser cavity. The gain is treated through an induced field polarization, capable of accurately describing a homogeneously broadened Lorentzian gain medium [36] and it is rigorously incorporated in our framework through first-order perturbation theory [37]. The carrier dynamics are included through semiclassical carrier rate equations. Using the framework, we thoroughly evaluate the effect

of the main physical system parameters on the lasing performance (CW and pulsed operation) and outline generic design directives to maximize lasing efficiency. Finally, we discuss the likelihood of multimode lasing in our proposed cavity through an evaluation of all the supported modes inside the luminescence spectrum of the TMD bilayer. In this work we study a single integrated lasing cavity; however, the coupled-mode-theory approach is naturally suited to the study of coupled oscillating cavities, which can produce rich physical phenomena [38–40], and to free-space or metasurface lasing structures [41].

The rest of the paper is organised as follows. In Sec. II, the developed CMT framework is presented in detail for a general three-level gain medium. General design directives and CW design metrics are extracted in order to guide the design process. In Sec. III, an initial evaluation of the framework is conducted by assuming a generic resonant structure, targeting to highlight the effect of each fundamental parameter on the overall response of a laser cavity and provide physical insight. In Sec. IV, the developed framework is applied in designing a practical laser cavity based on a MoS<sub>2</sub>/WSe<sub>2</sub>-enhanced SRNOI disk; its response is thoroughly assessed in both CW and pulsed operation. Finally, Sec. V offers concluding remarks.

## II. COUPLED-MODE-THEORY FRAMEWORK FOR PHOTONIC RESONATORS WITH GAIN

In this section, we present the developed framework, which rigorously introduces gain in the CMT formalism. Coupled-mode theory treats the cavity as a lumped oscillator, removing the spatial dimensions and leading to a mathematical representation in terms of ordinary differential equations (ODEs) with respect to time [29]. The physical characteristics of the three-dimensional (3D) cavity are incorporated into the coefficients of the first-order ODEs [37]. Naturally, this approach results in a very computationally efficient, but also quite accurate, framework [32,33], when the dimensions of the cavity are small enough so that the time that light needs for a single round trip is negligible compared to the photon lifetime of the cavity [29]. The developed framework is appropriate for any three-level system and can model either bulk or contemporary sheet-type gain materials. It is also readily adaptable to modifications regarding either the gain material itself (inclusion of other emission processes or phenomena, or additional energy levels) or other phenomena in the cavity (inclusion of nonlinearities, e.g., the Kerr effect or saturable absorption).

### A. Cavity-amplitude, polarization, and carrier-rate dynamic equations

To extract the coupled-mode-theory (cavity-amplitude) ODE, we begin from the Maxwell curl equations for nonmagnetic and nondispersive isotropic background

materials in the time domain:

$$\nabla \times \mathcal{E}(\mathbf{r}, t) = -\mu_0 \frac{\partial \mathcal{H}(\mathbf{r}, t)}{\partial t}, \quad (1a)$$

$$\nabla \times \mathcal{H}(\mathbf{r}, t) = \varepsilon_0 \varepsilon_r \frac{\partial \mathcal{E}(\mathbf{r}, t)}{\partial t} + \frac{\partial \mathcal{P}(\mathbf{r}, t)}{\partial t}. \quad (1b)$$

In Eq. (1b),  $\mathcal{P}(\mathbf{r}, t)$  is the polarization field induced by the light emission process (the dielectric properties of the involved materials are represented by  $\varepsilon_r$ ). When the emitter is a 2D material,  $\mathcal{P}(\mathbf{r}, t)$  contains only components tangential to the sheet. In Eq. (1) we express each field quantity using a slowly varying envelope and a reference or “carrier” frequency  $\Omega$  in the optical spectrum. Under this transformation, the electric field takes the form  $\mathcal{E}(\mathbf{r}, t) = \text{Re}\{\mathbf{E}(\mathbf{r}, t)e^{j\Omega t}\}$ , and similar expressions hold for  $\mathcal{H}(\mathbf{r}, t)$  and  $\mathcal{P}(\mathbf{r}, t)$ . Equations (1) then become

$$\nabla \times \mathbf{E}(\mathbf{r}, t) = -\mu_0 \left( \frac{\partial \mathbf{H}(\mathbf{r}, t)}{\partial t} + j\Omega \mathbf{H}(\mathbf{r}, t) \right), \quad (2a)$$

$$\nabla \times \mathbf{H}(\mathbf{r}, t) = \varepsilon_0 \varepsilon_r \left( \frac{\partial \mathbf{E}(\mathbf{r}, t)}{\partial t} + j\Omega \mathbf{E}(\mathbf{r}, t) \right) + \frac{\partial \mathbf{P}(\mathbf{r}, t)}{\partial t} + j\Omega \mathbf{P}(\mathbf{r}, t), \quad (2b)$$

where we have separated the terms oscillating at the positive and negative frequencies  $\pm\Omega$  and presented only the former. We then use a standard Fourier transform around the baseband frequency  $\zeta$  in Eqs. (2) so that, for example, the electric field in the frequency domain is  $\tilde{\mathbf{E}}(\mathbf{r}, \zeta) = \int \mathbf{E}(\mathbf{r}, t)e^{-j\zeta t} dt$ . Equations (2) then become

$$\nabla \times \tilde{\mathbf{E}}(\mathbf{r}, \zeta) = -j\mu_0(\Omega + \zeta)\tilde{\mathbf{H}}(\mathbf{r}, \zeta), \quad (3a)$$

$$\nabla \times \tilde{\mathbf{H}}(\mathbf{r}, \zeta) = j\varepsilon_0 \varepsilon_r (\Omega + \zeta)\tilde{\mathbf{E}}(\mathbf{r}, \zeta) + j(\Omega + \zeta)\tilde{\mathbf{P}}(\mathbf{r}, \zeta). \quad (3b)$$

The form of Eqs. (3) is very useful for the development of the CMT framework, as will become evident in what follows.

Next, we focus on the contribution of the emission-induced polarization field in the resonant cavity. In the process, we will use first-order perturbation theory [37], i.e., we will assume that the emission perturbs the resonance characteristics of the cavity (resonance frequency  $\omega_c$  and quality factor  $Q$ ) but leaves the field profiles mostly unaffected. This is a standard approach used to calculate the contribution of linear and/or nonlinear effects, on the basis that the approximate solution of a complex problem can be found starting from the exact solution of a closely matching, yet simpler, one. Perturbation theory is widely used in photonics and electromagnetics and it has been repeatedly found to lead to quite accurate results [42].

We start by using the index “0” to denote the unperturbed resonant system (i.e., a cavity with resonance frequency  $\omega_{c,0}$  in the absence of emission,  $\tilde{\mathbf{P}} = 0$ ) and define

the vector function  $\tilde{\mathbf{F}}_c = \tilde{\mathbf{E}}_0^* \times \tilde{\mathbf{H}} + \tilde{\mathbf{E}} \times \tilde{\mathbf{H}}_0^*$  [32], connecting the unperturbed problem with the perturbed one. For the perturbed system, and since the lasing frequency  $\omega_L$  is in general unknown, we introduce an arbitrary reference (“carrier”) frequency  $\omega_{\text{ref}}$  so that the perturbed Maxwell curl equations (3) are

$$\nabla \times \tilde{\mathbf{E}} = -j\mu_0(\omega_{\text{ref}} + \zeta)\tilde{\mathbf{H}}, \quad (4a)$$

$$\nabla \times \tilde{\mathbf{H}} = j\varepsilon_0 \varepsilon_r (\omega_{\text{ref}} + \zeta)\tilde{\mathbf{E}} + j(\omega_{\text{ref}} + \zeta)\tilde{\mathbf{P}}. \quad (4b)$$

Note that we have used here the symbol  $\omega_{\text{ref}}$  instead of the generic  $\Omega$ . On the other hand, the unperturbed versions of Eqs. (3) simply read

$$\nabla \times \tilde{\mathbf{E}}_0 = -j\mu_0(\omega_{c,0} + \zeta)\tilde{\mathbf{H}}_0, \quad (5a)$$

$$\nabla \times \tilde{\mathbf{H}}_0 = j\varepsilon_0 \varepsilon_r (\omega_{c,0} + \zeta)\tilde{\mathbf{E}}_0. \quad (5b)$$

Also note that in the notation of Eqs. (4) and (5) we have dropped the spectral and spatial arguments from the field quantities for brevity. The involved quantities are to be distinguished through, for example, the use of tildes and/or appropriate subscripts, but we will reinstate the respective arguments when deemed necessary. The divergence of  $\tilde{\mathbf{F}}_c$  is then found to be

$$\begin{aligned} \nabla \cdot \tilde{\mathbf{F}}_c &= -j\mu_0(\omega_{\text{ref}} - \omega_{c,0})\tilde{\mathbf{H}} \cdot \tilde{\mathbf{H}}_0^* \\ &\quad - j\varepsilon_0 \varepsilon_r (\omega_{\text{ref}} - \omega_{c,0})\tilde{\mathbf{E}} \cdot \tilde{\mathbf{E}}_0^* \\ &\quad - j(\omega_{\text{ref}} + \zeta)\tilde{\mathbf{P}} \cdot \tilde{\mathbf{E}}_0^*. \end{aligned} \quad (6)$$

To proceed, it is necessary to disentangle the spectral and spatial dependences of the involved fields through [33]

$$\tilde{\mathbf{E}}(\mathbf{r}, \zeta) = \tilde{A}(\zeta)\tilde{\mathbf{E}}_{\text{ref}}(\mathbf{r}), \quad (7a)$$

$$\tilde{\mathbf{H}}(\mathbf{r}, \zeta) = \tilde{A}(\zeta)\tilde{\mathbf{H}}_{\text{ref}}(\mathbf{r}), \quad (7b)$$

$$\tilde{\mathbf{P}}(\mathbf{r}, \zeta) = \tilde{P}(\zeta)\tilde{\mathbf{E}}_{\text{ref}}(\mathbf{r}). \quad (7c)$$

For this procedure, we have introduced the reference fields  $\tilde{\mathbf{E}}_{\text{ref}}$  and  $\tilde{\mathbf{H}}_{\text{ref}}$ , which are proportional to the mode profile of the unperturbed resonance (with resonance frequency  $\omega_{c,0}$ ) and are normalized to carry unitary energy, i.e., such that  $(1/4) \int_V (\varepsilon_0 \varepsilon_r |\tilde{\mathbf{E}}_{\text{ref}}|^2 + \mu_0 |\tilde{\mathbf{H}}_{\text{ref}}|^2) dV = 1$  [33]. These reference fields are typically obtained by numerically solving an eigenvalue problem of the resonant system.

Note that the designation “reference” in these field quantities should not be connected with the reference frequency  $\omega_{\text{ref}}$ , which is a “carrier” frequency chosen arbitrarily. As first-order perturbation theory implies, it is assumed that the reference fields are approximately the same in the unperturbed and perturbed systems, thus the subscript “0” is dropped throughout. It is the amplitudes  $\tilde{A}(\zeta)$  and

$\tilde{P}(\zeta)$  that embody the differences between the two systems. Inserting Eq. (7) into Eq. (6) results in

$$\begin{aligned} \nabla \cdot \tilde{\mathbf{F}}_c = & \\ & -j(\omega_{\text{ref}} - \omega_{c,0})\tilde{A}(\zeta)\tilde{A}_0^*(\zeta) \left[ \mu_0 |\tilde{\mathbf{H}}_{\text{ref}}|^2 + \varepsilon_0 \varepsilon_r |\tilde{\mathbf{E}}_{\text{ref}}|^2 \right] \\ & -j(\omega_{\text{ref}} + \zeta)\tilde{P}(\zeta)\tilde{A}_0^*(\zeta) |\tilde{\mathbf{E}}_{\text{ref}}|^2. \end{aligned} \quad (8)$$

Finally, Eq. (8) is integrated over an arbitrary volume assuming low radiation in the surrounding surface, something that leads to  $\int_V \nabla \cdot \tilde{\mathbf{F}}_c dV = \oint_{\partial V} \tilde{\mathbf{F}}_c \cdot d\mathbf{S} \rightarrow 0$  [37].

Under these conditions, the resonance frequency shift  $\Delta\omega = \omega_{\text{ref}} - \omega_{c,0}$  (in general complex) is given by

$$\Delta\omega\tilde{A}(\zeta) = -\xi_1(\omega_{\text{ref}} + \zeta)\tilde{P}(\zeta), \quad (9)$$

where we have defined the confinement factor

$$\xi_1 = \frac{1}{4} \int_{V_g} |\tilde{\mathbf{E}}_{\text{ref}}|^2 dV, \quad (10)$$

which measures the overlap between the optical mode and the gain-material volume  $V_g$ . The introduction of  $V_g$  reflects the fact that the polarization field  $\tilde{\mathbf{P}}(\mathbf{r}, \zeta)$  is nonzero only inside the gain material.

Next, Eq. (9) is transformed to the time domain. Using  $a(t) = (1/2\pi) \int \tilde{A}(\zeta) e^{j\zeta t} d\zeta$ , we reach

$$\Delta\omega = j\xi_1 \frac{1}{a(t)} \left[ j\omega_{\text{ref}} p(t) + \frac{dp(t)}{dt} \right], \quad (11)$$

where the complex amplitudes  $a(t)$  and  $p(t)$  are the time-domain counterparts of  $\tilde{A}(\zeta)$  and  $\tilde{P}(\zeta)$ . Note that  $a(t)$  and  $p(t)$  are slowly varying envelopes with  $\omega_{\text{ref}}$  as their reference frequency, i.e., they are connected with the respective vector fields through  $\mathbf{E}(\mathbf{r}, t) = a(t)\mathbf{E}_{\text{ref}}(\mathbf{r})$  and  $\mathbf{P}(\mathbf{r}, t) = p(t)\mathbf{E}_{\text{ref}}(\mathbf{r})$ . We should highlight here that the spatial dependence of the problem is captured in a weighted sense by the confinement factor  $\xi_1$ . As will become evident below, this approach significantly simplifies the computational handling of the problem without restricting the validity of the results [32,33,35]. It also allows one to obtain design metrics and design directives, and to gain interesting physical insight.

The simplest form of the cavity-amplitude ODE using the CMT notation is [29,30]

$$\frac{d\alpha(t)}{dt} = j\omega_L \alpha(t) - \frac{1}{\tau_\ell} \alpha(t), \quad (12)$$

where  $\omega_L$  is the unknown lasing frequency and  $\tau_\ell$  is the cavity lifetime, composed by the intrinsic  $\tau_i$  and external (coupling)  $\tau_e$  lifetimes, which satisfy  $\tau_\ell = (1/\tau_i + 1/\tau_e)^{-1}$  [43]. For the perturbed system, we are obligated to use the

hot resonance frequency of the cavity  $\omega_c \equiv \omega_L$ , i.e., the (in general, time-dependent) frequency at which the cavity will lase. In this form, the lasing frequency is still unknown but it equals  $\omega_L = \omega_{c,0} + \Delta\omega$ , as dictated by perturbation theory, and  $\Delta\omega$  is given by Eq. (11). We are also obligated to write the cavity-amplitude ODE using the (perturbed) amplitude  $\alpha(t)$ , corresponding to the (perturbed) field  $\mathcal{E}(\mathbf{r}, t) = \alpha(t)\mathbf{E}_{\text{ref}}(\mathbf{r})$ , so that  $\alpha(t) = a(t)e^{j\omega_{\text{ref}}t}$ . We note here that  $\alpha(t)$  and  $a(t)$  are two different quantities; however,  $|\alpha(t)|^2 = |a(t)|^2$  and equals the stored energy in the cavity due to the normalization of the reference fields.

With these points in mind, it is now possible to introduce Eq. (11) into Eq. (12) and reach the more useful CMT form for the slowly varying amplitude  $a(t)$ :

$$\begin{aligned} \frac{da(t)}{dt} = & -j(\omega_{\text{ref}} - \omega_{c,0})a(t) - \frac{1}{\tau_\ell} a(t) \\ & - \xi_1 \left[ j\omega_{\text{ref}} p(t) + \frac{dp(t)}{dt} \right]. \end{aligned} \quad (13)$$

Equation (13) can be solved to calculate the cavity amplitude of the resonator using *cold* (i.e., unperturbed) cavity quantities ( $\omega_{c,0}$ ,  $\tau_\ell$ , and  $\xi_1$ ) and the arbitrary reference frequency  $\omega_{\text{ref}}$ , with any choice of  $\omega_{\text{ref}}$  reasonably close to the resonance frequency of the cavity  $\omega_{c,0}$  to be valid.

The necessity of the latter will become more evident in Sec. II B, but we should note here that it constitutes an important contribution of this work, since it provides the means to estimate  $\omega_L$  in the most general case where the cold resonance frequency of the cavity does not coincide with the atomic transition frequency of the gain material. In the presented form, Eq. (13) includes the contribution of the emission-induced polarization and should be accompanied by an exit-channel equation of the form  $s_{\text{out}}(t) = \mu a(t)$ , where  $\mu \propto \sqrt{1/\tau_e}$  is a parameter that describes the interaction between the output channel and the cavity [31]. For an alternative, but equivalent, form of Eq. (13), see Sec. S1.i of the Supplemental Material [44]. Equation (13) does not contain any readily available information regarding the lasing frequency  $\omega_L$ , which is unknown and should not be confused with the arbitrary reference frequency  $\omega_{\text{ref}}$  (see the discussion in Sec. S1.ii of the Supplemental Material [44]). In Sec. II B, we present a method to approximately estimate  $\omega_L$ .

The second step is to find a solely time-dependent expression for the polarization-field amplitude. The polarization field in a gain medium typically follows the equation of a homogeneously broadened Lorentzian oscillator [36], i.e.,

$$\begin{aligned} \frac{\partial^2 \mathcal{P}(\mathbf{r}, t)}{\partial t^2} + \Gamma_m \frac{\partial \mathcal{P}(\mathbf{r}, t)}{\partial t} + \omega_m^2 \mathcal{P}(\mathbf{r}, t) \\ = -\sigma_m \Delta N(\mathbf{r}, t) \mathcal{E}(\mathbf{r}, t). \end{aligned} \quad (14)$$

The parameters  $\omega_m$  and  $\Gamma_m$  are the central frequency and the linewidth of the atomic transition for the gain material (accounting for radiative and nonradiative decays, as well as any possible dephasing that may arise), respectively, while  $\Delta N(\mathbf{r}, t)$  is the population inversion. The coupling parameter  $\sigma_m = 3\omega_m \varepsilon_0 \varepsilon_m \lambda_m^3 / (4\pi^2 \tau_{\text{spont}})$  depends on the emission wavelength  $\lambda_m$  and the spontaneous emission rate  $1/\tau_{\text{spont}}$ , and characterizes the gain material [36].

Equation (14) is simplified by using  $\mathcal{P}(\mathbf{r}, t) = \text{Re}\{\mathbf{P}(\mathbf{r}, t)e^{j\omega_{\text{ref}}t}\}$  and separating the terms oscillating at  $\pm\omega_{\text{ref}}$ :

$$(\Gamma_m + j2\omega_{\text{ref}}) \frac{\partial \mathbf{P}}{\partial t} + (\omega_m^2 - \omega_{\text{ref}}^2 + j\omega_{\text{ref}}\Gamma_m) \mathbf{P} = -\sigma_m \Delta N \mathbf{E}. \quad (15)$$

In Eq. (15), the slowly varying envelope approximation has also been exploited for the quantity  $\mathbf{P}(\mathbf{r}, t)$  in order to omit the second-order derivative. The temporal and spatial dependences of the electromagnetic fields are then disentangled using the idea of Eq. (7). We use  $\mathbf{P}(\mathbf{r}, t) = p(t)\mathbf{E}_{\text{ref}}(\mathbf{r})$ , since the electric field is the only readily available unperturbed field that resembles the spatial distribution of the polarization [cf. the driving term of Eq. (14)]. Ultimately, Eq. (15) becomes

$$(\Gamma_m + j2\omega_{\text{ref}}) \frac{dp}{dt} \mathbf{E}_{\text{ref}} + (\omega_m^2 - \omega_{\text{ref}}^2 + j\omega_{\text{ref}}\Gamma_m) p \mathbf{E}_{\text{ref}} = -\sigma_m \Delta N a \mathbf{E}_{\text{ref}}, \quad (16)$$

or, by multiplying with  $\mathbf{E}_{\text{ref}}^*$ , spatially integrating over  $V_g$ , and normalizing with the quantity  $\int_{V_g} |\mathbf{E}_{\text{ref}}|^2 dV$ ,

$$\frac{dp(t)}{dt} + \frac{\omega_m^2 - \omega_{\text{ref}}^2 + j\omega_{\text{ref}}\Gamma_m}{\Gamma_m + j2\omega_{\text{ref}}} p(t) = -\frac{\sigma_m}{\Gamma_m + j2\omega_{\text{ref}}} \Delta \bar{N}(t) a(t). \quad (17)$$

In Eq. (17), the spatially averaged population inversion is given by

$$\Delta \bar{N}(t) = \frac{\int_{V_g} \Delta N(\mathbf{r}, t) |\mathbf{E}_{\text{ref}}(\mathbf{r})|^2 dV}{\int_{V_g} |\mathbf{E}_{\text{ref}}(\mathbf{r})|^2 dV}. \quad (18)$$

Note that the temporal and spatial dependence of  $\Delta N(\mathbf{r}, t)$  cannot be disentangled following an approach similar to that used for the vector fields, since no scalar quantity with a proportionality relation to  $\Delta N$  is available. Equation (17) is the second coupled ODE of our framework and it generalizes previous reports in the literature [35]: by introducing the reference frequency  $\omega_{\text{ref}}$ , we have allowed for an arbitrary relation between  $\omega_{c,0}$  and

$\omega_m$ . The typically considered, but rather restrictive, case so far has been  $\omega_{c,0} = \omega_m$ , which also implies that  $\omega_L = \omega_m$  (in this case, one simply chooses  $\omega_{\text{ref}} = \omega_m$ ). Furthermore, we have not made any assumption regarding the atomic transition linewidth being small compared to the respective central frequency. The commonly considered case is  $\Gamma_m \ll \omega_m$ ; this approximation, although true in most cases, would limit the generality of the framework.

Finally, the carrier population must be introduced in the CMT representation. We opt for a simple three-level system, which is, however, sufficient to describe the atomic transitions in TMD bilayer heterostructures as well as other contemporary gain materials. The set of carrier-rate equations is [35,36]

$$\frac{\partial N_3(\mathbf{r}, t)}{\partial t} = R_p [N_1(\mathbf{r}, t) - N_3(\mathbf{r}, t)] - \frac{N_3(\mathbf{r}, t)}{\tau_{32}}, \quad (19a)$$

$$\frac{\partial N_2(\mathbf{r}, t)}{\partial t} = \frac{1}{\hbar\omega_m} \mathcal{E}(\mathbf{r}, t) \cdot \frac{\partial \mathcal{P}(\mathbf{r}, t)}{\partial t} + \frac{N_3(\mathbf{r}, t)}{\tau_{32}} - \frac{N_2(\mathbf{r}, t)}{\tau_{21}}, \quad (19b)$$

$$\frac{\partial N_1(\mathbf{r}, t)}{\partial t} = -\frac{1}{\hbar\omega_m} \mathcal{E}(\mathbf{r}, t) \cdot \frac{\partial \mathcal{P}(\mathbf{r}, t)}{\partial t} + \frac{N_2(\mathbf{r}, t)}{\tau_{21}} - R_p [N_1(\mathbf{r}, t) - N_3(\mathbf{r}, t)], \quad (19c)$$

where  $R_p$  is the pumping rate ( $\text{s}^{-1}$ ),  $\tau_{ij}$  are the carrier relaxation times between levels  $i$  and  $j$ , and the total number of carriers  $N_{\text{tot}} = N_1 + N_2 + N_3$  is constant (no photobleaching).

By applying the same transformations as earlier and exploiting the rotating wave approximation, thus neglecting the terms oscillating at  $\pm 2\omega_{\text{ref}}$ , it is straightforward to reach the spatially averaged version of the carrier-rate equations, which are readily incorporated in the CMT framework:

$$\frac{d\bar{N}_3(t)}{dt} = R_p [\bar{N}_1(t) - \bar{N}_3(t)] - \frac{\bar{N}_3(t)}{\tau_{32}}, \quad (20a)$$

$$\frac{d\bar{N}_2(t)}{dt} = \frac{\xi_2}{\hbar\omega_m} \frac{1}{2} \text{Re} \left\{ \left[ j\omega_{\text{ref}} p(t) + \frac{dp(t)}{dt} \right] a^*(t) \right\} + \frac{\bar{N}_3(t)}{\tau_{32}} - \frac{\bar{N}_2(t)}{\tau_{21}}, \quad (20b)$$

$$\frac{d\bar{N}_1(t)}{dt} = -\frac{\xi_2}{\hbar\omega_m} \frac{1}{2} \text{Re} \left\{ \left[ j\omega_{\text{ref}} p(t) + \frac{dp(t)}{dt} \right] a^*(t) \right\} + \frac{\bar{N}_2(t)}{\tau_{21}} - R_p [\bar{N}_1(t) - \bar{N}_3(t)], \quad (20c)$$

where

$$\xi_2 = \frac{\int_{V_g} |\tilde{\mathbf{E}}_{\text{ref}}|^4 dV}{\int_{V_g} |\tilde{\mathbf{E}}_{\text{ref}}|^2 dV} \quad (21)$$

is a different confinement factor, not equal but similar to  $\xi_1$ . For the three-level system that we consider here, the population inversion takes place between levels 2 and 1, i.e.,  $\Delta\bar{N} = \bar{N}_2 - \bar{N}_1$  is to be used to couple Eqs. (20) with Eq. (17). We opted not to include an expression for  $\Delta\bar{N}$  earlier in Eq. (17) so that the transition to a system with different energy levels is facilitated.

Equations (13), (17), and (20) constitute the full set of the temporal CMT equations that accurately describe a three-level gain medium embedded in a resonant cavity and are actually quite general since they are extracted from the semiclassical Maxwell-Bloch equations, traditionally used to characterize lasers [36]. They can be easily expanded to more complex gain media with more energy levels [45] or they can include other nonlinear effects, such as saturable absorption [33] or the Kerr effect [32]. Importantly, they can also be used to describe contemporary 2D gain materials (TMDs, black phosphorus, etc.) by restricting the spatial integrations on the surface of the 2D material  $S_g$  and by using the tangential-to-the-sheet  $E$ -field components, i.e.,  $\tilde{\mathbf{E}}_{\text{ref},\parallel}$ . Specifically, the two confinement factors defined earlier become

$$\xi_1 = \frac{1}{4} \int_{S_g} |\tilde{\mathbf{E}}_{\text{ref},\parallel}|^2 dS, \quad (22a)$$

$$\xi_2 = \frac{\int_{S_g} |\tilde{\mathbf{E}}_{\text{ref},\parallel}|^4 dS}{\int_{S_g} |\tilde{\mathbf{E}}_{\text{ref},\parallel}|^2 dS}. \quad (22b)$$

Note that, in Eq. (22a), the units of  $\xi_1$  are reduced by  $m$ , which is consistent with the units of the *surface* carrier density, now measured per unit area (instead of per unit volume), and the *surface* polarization field, measured in C/m.

## B. Lasing characteristics and continuous-wave design metrics

For a general assessment of the performance of a lasing system, it is convenient to extract characteristic CW metrics. We start by determining the minimum required population inversion for lasing (population-inversion threshold) in the most convenient case where  $\omega_{c,0} = \omega_m = \omega_L$ . By removing the time derivatives in Eqs. (13) and (17), and by substituting the latter into the former, we get

$$\Delta\bar{N}_{\text{th}} = \frac{\Gamma_m}{\sigma_m \xi_1 \tau_\ell}. \quad (23)$$

A low threshold is always desirable, thus the product  $\xi_1 \tau_\ell$ , which depends on the physical resonator, is to be maximized. This is our *first design metric*.

Following the same approach, but examining the more general case when  $\omega_{\text{ref}} \neq \omega_{c,0} \neq \omega_m$ , we find

$$\Delta\bar{N}_{\text{th}} = \frac{j(\omega_{\text{ref}} - \omega_{c,0})\tau_\ell + 1}{j\omega_{\text{ref}}\sigma_m \xi_1 \tau_\ell} (\omega_m^2 - \omega_{\text{ref}}^2 + j\omega_{\text{ref}}\Gamma_m), \quad (24)$$

which should always be a real quantity since it represents a difference in carrier population densities. Thus, by requiring the imaginary part to be zero, we find that

$$\omega_L = \frac{\Gamma_m \tau_\ell \omega_{c,0} \pm \sqrt{(\Gamma_m \tau_\ell \omega_{c,0})^2 + 4(1 + \Gamma_m \tau_\ell)\omega_m^2}}{2(1 + \Gamma_m \tau_\ell)}, \quad (25)$$

which proves to be a very good estimate of the lasing frequency. Note that, when requiring  $\text{Im}\{\Delta\bar{N}_{\text{th}}\} = 0$ , one should treat  $\omega_{\text{ref}}$  as the lasing frequency  $\omega_L$  to obtain Eq. (25). This correspondence stems from the physical restriction of  $\Delta\bar{N}_{\text{th}}$  being real and, thus, the resulting frequency should hold a physical meaning as well. Still, Eq. (25) does not set any restriction on the choice of  $\omega_{\text{ref}}$  when applying the framework; any reasonable  $\omega_{\text{ref}}$  is valid but, when  $\omega_{\text{ref}} \neq \omega_L$ , oscillations on the complex amplitudes  $a(t)$  and  $p(t)$  will emerge at steady state. The CW response of the system remains unchanged. A more in-depth discussion regarding the various choices of  $\omega_{\text{ref}}$  and their consequences can be found in Sec. S1.ii of the Supplemental Material [44].

Another useful quantity is the pumping-rate threshold  $R_{p,\text{th}}$ , which is easily extracted from Eqs. (20) under CW operation when additionally  $\tau_{32} \ll \tau_{21}$  (i.e., the second level being metastable), which should hold for any gain material in order to achieve population inversion. It equals

$$R_{p,\text{th}} = \frac{1}{\tau_{21}} \frac{\bar{N}_{\text{tot}} + \Delta\bar{N}_{\text{th}}}{\bar{N}_{\text{tot}} - \Delta\bar{N}_{\text{th}}}, \quad (26)$$

and when  $\bar{N}_{\text{tot}} \gg \Delta\bar{N}_{\text{th}}$ , another typical scenario for lasing, it equals  $1/\tau_{21}$ . On the other hand, when  $\Delta\bar{N}_{\text{th}} \rightarrow \bar{N}_{\text{tot}}$ ,  $R_{p,\text{th}} \rightarrow \infty$  and lasing is suppressed.

Finally, another useful simplified expression is the one that allows the calculation of the output power  $P_{\text{out}} = \mu^2 |a|^2$  under CW conditions when  $\omega_{c,0} = \omega_m = \omega_L$ :

$$P_{\text{out}} = \mu^2 \frac{2\hbar\omega_m \tau_\ell \xi_1}{\xi_2} \left( \frac{\bar{N}_3}{\tau_{32}} - \frac{\bar{N}_2}{\tau_{21}} \right), \quad (27)$$

with

$$\bar{N}_3 = \frac{\bar{N}_{\text{tot}} - \Delta\bar{N}_{\text{th}}}{3 + 2/(R_p \tau_{32})}, \quad (28a)$$

$$\bar{N}_2 = \Delta\bar{N}_{\text{th}} + \left( 1 + \frac{1}{R_p \tau_{32}} \right) \bar{N}_3. \quad (28b)$$

From Eq. (27) one can readily see that  $P_{\text{out}} \propto \tau_\ell \xi_1 / \tau_e \xi_2$  since  $\mu^2 \propto 1/\tau_e$ . Usually,  $\tau_e \ll \tau_i$  to favor light coupling

to the outside world and thus  $\tau_c/\tau_e \approx \tau_e/\tau_e = 1$ . To further increase  $P_{\text{out}}$ , one has to maximize the  $\xi_1/\xi_2$  ratio. This constitutes our *second design metric*.

As a concluding remark of this section, we compile the new contributions of the proposed framework. The detailed derivation and the careful development of the framework has allowed the cavity and atomic transition frequencies to be treated independently ( $\omega_m$  and  $\omega_{c,0}$  do not have to coincide) and furthermore resulted in a closed-form (approximate yet quite accurate) expression to estimate  $\omega_L$ , without resorting to the more rigorous, but also more cumbersome, steady-state *ab initio* laser theory [46]. The framework is developed in an easily expandable way, highlighted in this work by the minimal adjustments needed to include 2D gain materials. Finally, through realistic simplifications, the framework led to useful CW design metrics for minimizing the population-inversion threshold and maximizing the lasing output power. In the remainder of the paper, we focus on how the framework can be further utilized to extract useful design directives towards the design of efficient integrated cavities and be exploited to assess their lasing performance in dynamic conditions.

### III. ASSESSING CONTINUOUS-WAVE PERFORMANCE AND DEFINING DESIGN DIRECTIVES

As an initial evaluation of the developed framework, we examine the behavior of an abstract cavity, enhanced with a gain material. Our focus here is to extract general trends; thus, we examine the output power expressed in arbitrary units and the pumping strength expressed in units of  $1/\tau_{21}$  [cf. Eq. (26)]. Furthermore, we focus on the optimum choice of  $\omega_{c,0} = \omega_m$  and examine a system with  $\Delta\bar{N}_{\text{th}} \ll \bar{N}_{\text{tot}}$ . These conditions are indicative of most practical systems, thus they are adopted throughout this general evaluation, unless otherwise mentioned. To extract the results discussed below and in the case that  $\omega_{c,0} = \omega_m$ ,

one might use either the full system [Eqs. (13), (17), and (20)] when the time derivatives are dropped or the closed-form relations [Eqs. (23), (27), and (28)]. On the other hand, when  $\omega_{c,0} \neq \omega_m$ , the full system has to be utilized without dropping the time derivatives due to the emerging oscillations on the complex amplitudes of  $a(t)$  and  $p(t)$ , in the general case that  $\omega_L \neq \omega_{\text{ref}}$  (see Sec. S1 of the Supplemental Material [44]).

First, we focus on the coupling strength between the light-emitting cavity and the bus waveguide. In normalized terms, the strength of this process is governed by the ratio of intrinsic and external quality factors,  $r_Q = Q_i/Q_e$ . The results of Fig. 1(a) validate the physical intuition that, indeed, a greater  $r_Q$  (for the same  $R_p$  input) results in stronger coupling and thus higher output power is coupled to the bus waveguide. However, after some point, the increase in  $r_Q$  leads to only a minor increase of the power coupled to the bus waveguide, since practically all of the light emitted from the TMD inside the cavity is coupled to the bus waveguide. Thus, an  $r_Q > 10$  is practically unnecessary. This is better imprinted in the inset, where it is easily observed that the slope of the light-light curves ( $\partial P_{\text{out}}/\partial R_p$ ) approaches a constant value as  $r_Q$  increases. On the hand, the choice of  $r_Q$  does not impact  $R_{p,\text{th}}$ , at least for the case considered here where  $\Delta\bar{N}_{\text{th}} \ll \bar{N}_{\text{tot}}$  [cf. Eq. (26)]. Consequently, the choice of  $r_Q = 10$  will be used hereafter as the “benchmark” value. This choice can be considered a *design directive* that we anticipate will find application also in other integrated laser cavities based on traveling-wave resonators. Finally, we should note that a clear gain saturation is observed as  $R_p$  grows beyond  $10^3$  in Fig. 1(a), a well-expected behavior for any laser [36]. Even so, the light-light curve is linear for an  $R_p$  span of approximately 3 orders of magnitude.

Secondly, we shift the resonance frequency of the cavity so that now  $\omega_{c,0} \neq \omega_m$  and record the output power at the respective *hot* resonance frequency  $\omega_c \equiv \omega_L$ . Equation (25) is used to estimate this frequency, which in the cases

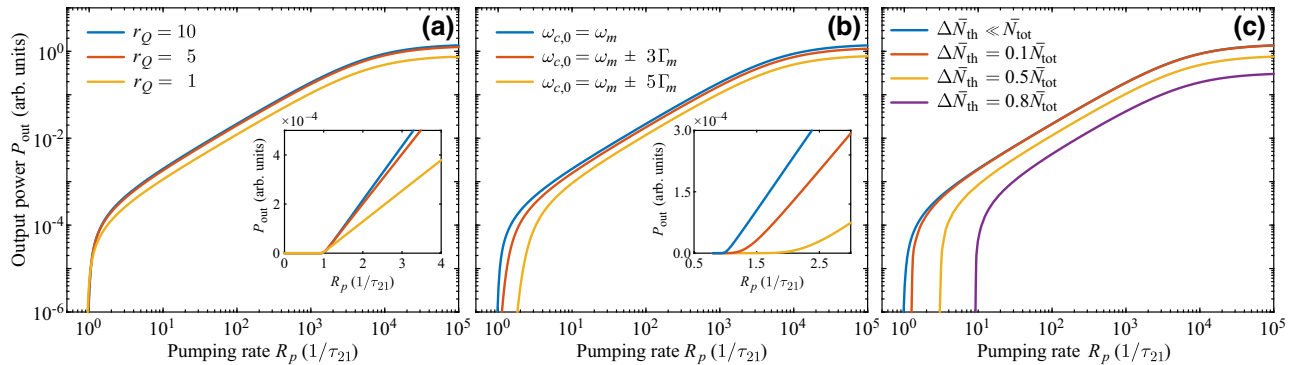


FIG. 1. Performance evaluation of a generic traveling-wave laser cavity in terms of the coupled power to the bus waveguide with respect to some fundamental parameters: (a) coupling strength,  $r_Q$  parameter (inset: linear scale close to threshold); (b) unperturbed resonance frequency,  $\omega_{c,0}$  parameter (inset: linear scale close to threshold); and (c) population-inversion threshold,  $\Delta\bar{N}_{\text{th}}$  parameter. The three panels reveal interesting directives for the design of integrated laser cavities.

examined lies quite close to  $\omega_{c,0}$ , as intuitively expected. The results of Fig. 1(b) show that, as the two frequencies deviate, the pumping-strength threshold increases and less power is emitted and coupled to the bus waveguide. Both findings are reasonable since the gain material has a Lorentzian emission spectrum and thus less light is emitted as  $\omega_L$  (which is close to  $\omega_{c,0}$ ) deviates from  $\omega_m$ . Nevertheless, when the *cold* resonance frequency of the cavity lies within the range  $\omega_m \pm 3\Gamma_m$ , the negative impact of this detuning between  $\omega_{c,0}$  and  $\omega_m$  is benign. More specifically, from the inset of Fig. 1(b), the pumping-rate threshold is higher by at most 25%. This fact is also a useful *design directive*, allowing for some extra freedom in the design of the resonant cavity taking manufacturing tolerances into account.

Finally, we modify the system parameters so that the population-inversion threshold needed for emission grows closer to the total available carriers in the gain material, i.e.,  $\Delta\bar{N}_{\text{th}} \rightarrow \bar{N}_{\text{tot}}$ . The curves depicted in Fig. 1(c) validate the accuracy of Eq. (26), which correctly predicts the pumping-strength threshold for emission. Furthermore, the light emitted is significantly weaker as the population-inversion threshold approaches the total available number of carriers. We find that a population-inversion threshold as high as 10% of the total available carriers mostly reproduces the emission characteristics of the benchmark example ( $\Delta\bar{N}_{\text{th}} \ll \bar{N}_{\text{tot}}$ ); the only difference is  $R_{p,\text{th}}$  being 20% higher. This is another *design directive*. Population threshold conditions up to  $\Delta\bar{N}_{\text{th}} \leq 0.1\bar{N}_{\text{tot}}$  do not affect the output power and they can be allowed in a practical design if the penalty on the pumping-strength threshold can be tolerated.

#### IV. DESIGN AND PERFORMANCE OF AN INTEGRATED MICRODISK OVERLAID WITH TMD HETEROSTRUCTURE

Having presented the theoretical framework, and following the preliminary CW assessment in the previous sections, we proceed to the complete numerical study and design of a laser cavity incorporating a TMD bilayer heterostructure as the active medium. The vertical stacking of two TMD monolayers creates a type-II band alignment heterostructure [15], which leads to a number of highly favorable optoelectronic properties. Most notably, the emission wavelength depends on the energy levels of the individual TMD monolayers [15], while it can also be electrically adjusted through the Stark effect by applying an external static electric field perpendicularly polarized to the plane of the heterostructure [14–16]. The latter is a result of the spatial separation of the electrons and holes in different TMD monolayers (see the discussion below). Therefore, TMD bilayer heterostructures can be exploited in practical optical sources covering a wide and adjustable spectral range in the NIR. The most well-studied TMD

bilayers are the MoS<sub>2</sub>/WSe<sub>2</sub> [14,17,19] and MoSe<sub>2</sub>/WSe<sub>2</sub> [20,21] heterostructures, which have also been exploited recently in novel laser cavities [22,23]. In this work, we choose the MoS<sub>2</sub>/WSe<sub>2</sub> bilayer, since its emission wavelength is found to be in the range 1240–1127 nm (1.0–1.1 eV) [14], hence in the lower limit of the O band for communications, in contrast with the MoSe<sub>2</sub>/WSe<sub>2</sub> heterostructure, which emits light around 890 nm (1.4 eV) [20,21].

The photoluminescence process of the MoS<sub>2</sub>/WSe<sub>2</sub> heterostructure is schematically illustrated in Fig. 2(a). We note that fundamentally the photoluminescence process is the same for every TMD bilayer heterostructure [14–21]. Initially, the bilayer is illuminated by a pump wave with wavelength  $\lambda_p = 740$  nm equal to the A exciton of the WSe<sub>2</sub> monolayer transition energy [47], resulting in the photogeneration of intralayer excitons. Subsequently, the type-II band alignment of the heterostructure results in an ultrafast electron transfer from the conduction band of WSe<sub>2</sub> to the empty conduction band of MoS<sub>2</sub> with the relaxation time evaluated in the range 1–100 fs [15]. Concurrently, the intralayer exciton photoluminescence in the WSe<sub>2</sub> is strongly quenched, as it is characterized by a recombination lifetime of a few picoseconds [10,15], thus much slower than the electron transfer process. *Interlayer* excitons are formed between the conduction band of MoS<sub>2</sub> and the valence band of WSe<sub>2</sub>, which recombine at a much slower, nanosecond, time scale [16], allowing for population inversion to be achieved.

It is important to note that the emission properties of the TMD heterostructures are strongly dependent on the twist angle between the individual monolayers [15,16]. Hence, the individual TMD monolayers have to be closely aligned crystallographically, enabling the interlayer excitons to recombine predominantly radiatively (bright excitons) [14,22], which is a prerequisite for lasing devices. On the contrary, when the individual TMD monolayers are misaligned, radiative recombination is not observed (dark excitons) and the TMD bilayer cannot be exploited for practical lasing structures [14].

The considered MoS<sub>2</sub>/WSe<sub>2</sub> bilayer can be modeled as a three-level gain medium, with levels 1, 2, and 3 being the valence band of WSe<sub>2</sub>, the conduction band of MoS<sub>2</sub>, and the conduction band of WSe<sub>2</sub>, respectively; the conditions for achieving population inversion between levels 1 and 2 are satisfied. In this work, we set the electron relaxation time from the conduction band of WSe<sub>2</sub> to the conduction band of MoS<sub>2</sub> equal to  $\tau_{32} = 100$  fs. We have checked that any choice inside the typically quoted range of 1–100 fs negligibly influences the system. The spontaneous-emission lifetime (radiative interlayer-exciton recombination time) is  $\tau_{\text{spon}} = 1$  ns and is assumed here to be equal to  $\tau_{21}$ . Spontaneous emission is known to significantly affect light emission around the lasing threshold in microlasers [11,13,23,48], in contrast to

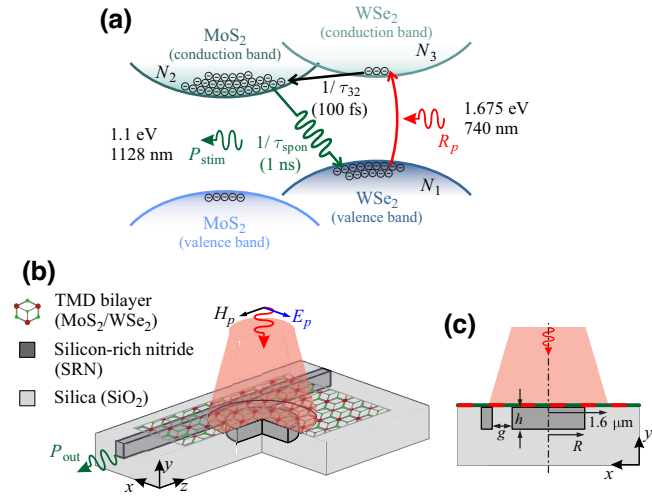


FIG. 2. (a) The three-level energy diagram of the  $\text{MoS}_2/\text{WSe}_2$  heterostructure, which allows for stimulated emission at 1128 nm due to radiative recombination of interlayer excitons formed between the conduction band of  $\text{MoS}_2$  and the valence band of  $\text{WSe}_2$ . (b) A 3D schematic of the proposed laser structure consisting of a disk resonator side-coupled to a bus waveguide with the TMD bilayer residing on top. The vertical pump illumination and the output channel are both clearly illustrated. (c) An  $x$ - $y$  cut of the proposed laser cavity showing the various geometric parameters and the vertical pump illumination area.

typical large-scale lasers. Nevertheless, here we focus on the more fundamental process of stimulated emission and leave the influence of spontaneous emission to be examined in future work. The central emission wavelength of the TMD bilayer is  $\lambda_m = 1128$  nm [23], while its linewidth is found in the order of terahertz [14,23,49]. For this study, we choose a typical value of  $\Gamma_m = 20$  Trad/s. The spatially averaged total surface carrier density is set to  $\bar{N}_{\text{tot}} = 10^{13} \text{ cm}^{-2}$  [50].

The laser structure under study is schematically depicted in Figs. 2(b) and 2(c), consisting of a silica-clad silicon-rich nitride (SRN) disk resonator with radius  $R$  and height  $h$ . The cavity supports well-confined whispering-gallery modes with high quality factors which favor efficient lasing. The TMD bilayer resides on top of the structure and in direct contact with the disk resonator, maximizing field overlap with the 2D material. The resonator is side-coupled to a bus waveguide at a distance  $g$ , enabling the extraction of emitted light to the waveguide. The proposed laser configuration can be exploited for on-chip integration with other optical components. The width of the waveguide is set to  $w_{\text{wg}} = 130$  nm and  $h$  acquires values around 300 nm ( $h$  is a design parameter, thus its exact value will be determined in what follows). Since the cross-sectional dimensions are small and  $h > w_{\text{wg}}$ , only the fundamental quasi-TM mode ( $\text{TM}_{00}$ ) is supported. Note that quasi-TM modes are characterized by  $E_y$  being the

dominant transverse [i.e., lying in the cross-sectional  $x$ - $y$  plane; see Fig. 2(b)] electric field component.

The TMD bilayer is optically pumped with a normally incident free-space beam, as illustrated in Figs. 2(b) and 2(c). We note that the SRNOI platform has been chosen instead of the standard SOI, since the large band gap of SRN prohibits one-photon absorption even for the pump wave ( $\mathcal{E}_g^{\text{SRN}} = 2.05$  eV, corresponding to absorption below 605 nm). In contrast, the band gap of silicon lies in the vicinity of the emission wavelength, resulting in substantial losses of the emitted light and, thus, impeding lasing operation. We have opted for a high Si:N ratio, resulting in high refractive index, close to that of Si, enabling miniaturization and strong field confinement in the proposed nanophotonic device. Overall, the chosen SRNOI platform is meant to strike a favorable balance between the characteristics of SOI and SNOI platforms.

In the wavelength region of  $\lambda_m$ , we have  $n_{\text{SRN}} = 3.15 - j10^{-5}$  [25] and  $n_{\text{SiO}_2} = 1.45$ . The small imaginary part in the refractive index of SRN has been heuristically introduced to accommodate in a phenomenological manner every kind of defect and loss that restrains the intrinsic quality factor, setting an upper limit of  $Q_{\text{res}} \sim 170\,000$ ; this limit is quite high and does not affect the validity of the developed coupled-mode-theory framework [32]. If losses were significant, an alternative derivation based on an unconjugated form of the vector function  $\vec{F}_c$  would have to be followed [51]. Losses are also negligible for the individual monolayers which do not absorb light at the emission wavelength [47], since their band gaps ( $\mathcal{E}_g^{\text{WSe}_2} = 1.675$  eV and  $\mathcal{E}_g^{\text{MoS}_2} = 1.9$  eV) are much greater than the energy of the emitted photons at  $\lambda_m$  (1.1 eV). Therefore, their surface conductivities are purely imaginary and can be described through the reported effective refractive indices in the literature using  $\sigma = j\omega\epsilon_0 d_{\text{TMD}}(n_{\text{TMD}}^2 - 1)$ . Consequently, the surface conductivities are  $\sigma_{\text{MoS}_2} = j167 \mu\text{S}$  and  $\sigma_{\text{WSe}_2} = j202 \mu\text{S}$  at the emission wavelength [52]. The total surface conductivity of the bilayer is the sum of the two individual values, i.e.,  $\sigma_{\text{bilayer}} = \sigma_{\text{MoS}_2} + \sigma_{\text{WSe}_2} = j369 \mu\text{S}$ . The purely imaginary surface conductivity of the bilayer results only in a redshift of the resonance wavelength. This shift is not negligible ( $\sim 2$  nm) as a result of the relatively high value of  $\sigma_{\text{bilayer}}$ .

Finally, to calculate the coupling parameter  $\sigma_m$  [cf. Eq. (14)] we have used an approximate value of the refractive index for the gain material,  $n_{\text{TMD}} \sim 4.5$ , which is in between the actual refractive indices of the monolayers ( $n_{\text{WSe}_2} = 4.7$  and  $n_{\text{MoS}_2} = 4.4$ ) [52] used to extract the aforementioned surface conductivities and thus obtain the value of  $\sigma_m = 3.58 \times 10^{-7} \text{ C}^2/\text{kg}$ . It is also important to note that SRN exhibits a high nonlinear refractive index, which is an order of magnitude greater than that of Si [25]. Nevertheless, our calculations indicate that the influence of the Kerr effect induced by SRN, for the considered range of pump powers, is negligible and thus it has been

omitted from the equations and the subsequent calculations throughout this work.

To assess the operation of the proposed laser element, it is crucial to relate the pumping strength  $R_p$  with the pumping power  $P_p$  that illuminates the TMD bilayer. This is typically done through  $P_p = \hbar\omega_p V_g \bar{N}_1 R_p / \eta_p$  [35,36], where  $\omega_p$  is the pumping angular frequency. When  $\Delta\bar{N}_{\text{th}} \ll \bar{N}_{\text{tot}}$ , we have approximately  $\bar{N}_1 \approx \bar{N}_{\text{tot}}/2$ , further simplifying the aforementioned relation. Nevertheless, due to the 2D nature of the gain material, the volume  $V_g$  is reduced to a surface  $S_g$ , with  $\bar{N}_{\text{tot}}$  reducing to a (spatially averaged) surface carrier density, measured in carriers per square meter. Henceforth, we assume that the active surface is circular (as the spot of the pumping beam would be) with radius  $1.6 \mu\text{m}$ , which is always greater than the radius  $R$  of the resonator that we study below. Furthermore,  $\eta_p$  is the absorption efficiency of the WSe<sub>2</sub> monolayer and expresses the fraction of incident power that is absorbed by the monolayer.

Apart from the real part of the surface conductivity of WSe<sub>2</sub> at the pump wavelength, the underlying materials and structure, notably the height of the disk resonator, also greatly affect  $\eta_p$ . This is due to the formation of a Fabry-Perot-like cavity as the disk structure is vertically illuminated [cf. Fig. 2(c)]. In general, the absorption efficiency is point-dependent, i.e.,  $\eta_p \equiv \eta_p(\mathbf{r})$ , since the presence of the disk below the bilayer results in an inhomogeneous field distribution on the bilayer plane. Although a spatiotemporal version of the CMT can accommodate such an effect [53], here we opt for the simple scenario where  $\eta_p$  is estimated assuming uniform layers consisting (bottom to top) of silica, SRN, the TMD bilayer, and air [cf. inset of Fig. 4(b)]. This approach takes into account the nature of the underlying Fabry-Perot cavity (formed inside the SRN slab of height  $h$ ) and allows for the estimation of a worst-case-scenario  $\eta_p$ , since any lateral modulation of the SRN layer will further enhance the interaction of light with the 2D heterostructure (see Sec. S4 of the Supplemental Material [44] for more detailed results on  $\eta_p$  calculations). The refractive indices of the SRN and SiO<sub>2</sub> at the wavelength  $\lambda_p$  are  $n_{\text{SRN}} = 3.36$  [25] and  $n_{\text{SiO}_2} = 1.45$ , respectively, while the surface conductivities of the TMD monolayers are  $\sigma_{\text{WSe}_2} = 386 + j227 \mu\text{S}$  and  $\sigma_{\text{MoS}_2} = j347 \mu\text{S}$  [47]; note the presence of a real part in  $\sigma_{\text{WSe}_2}$ , indicating absorption.

Next, the overall response of the laser structure is examined by calculating the standard light-light curves that characterize the operation of optically pumped lasers. We meticulously investigate the effect of the geometrical parameters of the disk ( $R$  and  $h$ ) on the overall response, utilizing the two design metrics presented in Sec. II B. There is also a third geometric parameter, the coupling gap  $g$ , that needs to be specified, and this can be done in two ways: (i) adjusting  $g$  continuously as  $R$  and/or  $h$  are modified so that  $r_Q$  is fixed at a specified value; or

(ii) setting  $g = \text{const.}$  and thus having  $r_Q$  changing as  $R$  and/or  $h$  are tuned. Both of them lead to the same qualitative results (see Sec. S3.1 of the Supplemental Material [44]). We first conduct linear simulations utilizing the finite-element method (FEM) commercial software COMSOL Multiphysics® in order to extract the parameters and coefficients that feed the developed CMT framework, i.e.,  $\omega_{c,0}$ ,  $Q_i$ ,  $Q_e$ ,  $\xi_1$ , and  $\xi_2$ . Capitalizing on the discussion in Sec. III, we engineer the resonator geometrical parameters (mostly its radius  $R$ ) each time so that  $\lambda_{c,0} = \lambda_m$  and thus  $\lambda_L = \lambda_m$  as well. Then, we use either the full-system equations [Eqs. (13), (17), and (20)] or even the closed-form relations [Eqs. (23), (27), and (28)] to assess the overall response of the resonator.

The first geometric parameter to consider is the radius  $R$  of the resonator. To this end, we fix the height of the resonator to  $h = 340 \text{ nm}$  and change the radius  $R$ , hence modifying the azimuthal order  $m$  of the respective whispering-gallery mode (radial order  $q = 1$ ) that is found closest to the peak emission wavelength  $\lambda_m$ . As  $h$  is kept constant,  $\eta_p$  remains constant as well and equals  $\eta_p = 7.1\%$  (see Sec. S4 of the Supplemental Material [44]). Moreover, the ratio of the quality factors is assumed to be equal to its benchmark value of  $r_Q = 10$ , implying that the coupling gap  $g$  is adjusted for every mode considered.

The light-light curves are depicted in Fig. 3 for three modes of order  $m = \{12, 14, 16\}$ , associated with  $R = \{1.015 \mu\text{m}, 1.160 \mu\text{m}, 1.305 \mu\text{m}\}$ , respectively. As the mode order increases, radiative losses decrease and, therefore, the intrinsic quality factor rises [43]. Specifically, we have  $Q_{i,12} = 13\,300$ ,  $Q_{i,14} = 47\,500$ , and  $Q_{i,16} = 107\,500$  [see also Fig. S5(a) of the Supplemental Material [44]]. On the other hand,  $\xi_1$  decreases slightly as the mode order increases because of the stronger light confinement inside the cavity, which leads to a decrease of the interaction between the supported mode and the TMD bilayer. On the whole, the quantity  $1/\tau_\ell \xi_1$ , and therefore  $\Delta\bar{N}_{\text{th}}$ , decreases with  $m$ , resulting in lower pumping thresholds for larger values of  $R$ . Nonetheless, the required population inversion for lasing is in the order of  $10^{11} \text{ cm}^{-2}$  and thus  $\Delta\bar{N}_{\text{th}} \ll \bar{N}_{\text{tot}}$  [well below the 10% limit identified in Fig. 1(c)], resulting practically in the same pumping-power threshold, which is  $P_{p,\text{th}} \simeq 1.5 \text{ mW}$  [inset of Fig. 3]. Concurrently with the slight decrease of  $\xi_1$ , we obtain an expected decrease of  $\xi_2$  for higher radii. However,  $\xi_2$  decreases faster, leading to an overall increase of the quantity  $\xi_1/\xi_2$  with  $R$ . Therefore, as becomes obvious from Fig. 3, for the same  $P_p$  we get higher output power as the mode order increases. Traditionally, this is measured by the slope of the light-light curve, which is indeed higher for larger  $R$  [inset of Fig. 3]. Overall, we conclude that both design metrics set in Sec. II B improve by increasing  $R$  or, equivalently, the mode order  $m$  (see Sec. S3 of the Supplemental Material [44] for more details and results on the design process).

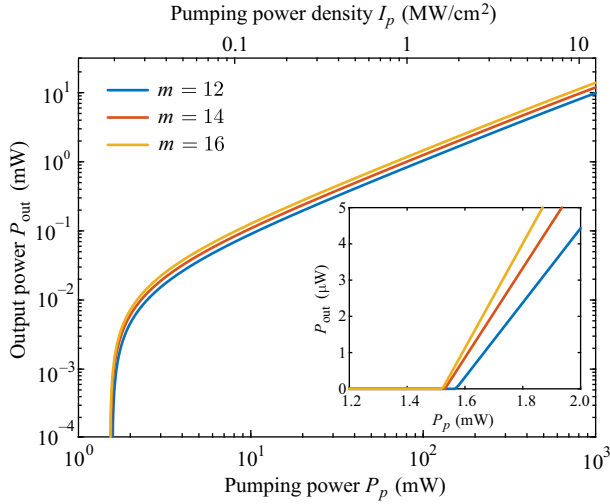


FIG. 3. Output power  $P_{\text{out}}$  versus pumping power  $P_p$  (or power density  $I_p = P_p/S_g$ ) as the (azimuthal) mode order  $m$  of the lasing whispering-gallery mode is engineered by properly adjusting the radius  $R$  of the resonator. The height of the cavity is constant at the typical value of  $h = 340$  nm and  $r_Q = 10$  for every mode considered. Inset: Enlarged view of the curves (linear scale) near the threshold to better illustrate that both the design metrics set in Sec. II B (lasing threshold and output power) are improving with increasing values of  $R$ .

The effect of the resonator height  $h$  is also assessed to seek the optimum design, while the order of the lasing mode is now kept constant at  $m = 16$ . The height of the cavity affects the mode confinement and consequently the quality factor as well as the interaction between the mode and the TMD bilayer. In addition, the choice of  $h$  plays an important role in the absorption of the incident pump light, as already discussed and to be presented below. To examine how  $h$  affects the lasing mode of the cavity, we first artificially fix  $\eta_p$  (i.e., the absorption coefficient) to its maximum value of 8.6% and study the trend of the two design metrics of Sec. II B. We also keep the coupling gap constant at the value  $g = 300$  nm and thus  $r_Q$  changes with  $h$ . We note that, as  $h$  is modified, the radius  $R$  of the resonator is also fine-tuned so that  $\lambda_{c,0} = \lambda_m = 1128$  nm (the azimuthal order of the lasing mode always remains the same).

In Fig. 4(a) the calculated light-light curves are depicted for four different values of  $h$ . An increase of  $h$  leads to a stronger confinement of the mode inside the cavity, resulting in higher values of  $Q_i$ . Furthermore,  $r_Q$  initially increases with  $h$  before reaching its benchmark value of  $r_Q = 10$ , at which it practically remains constant as  $h > 300$  nm [see Fig. S6(a) of the Supplemental Material [44]]. Therefore, the loaded quality factor  $Q_\ell$  increases with  $h$ . Concurrently, the light-TMD interaction decreases with  $h$ , leading to a substantial decrease of the two confinement factors  $\xi_1$  and  $\xi_2$ . We can now find the optimum height of

the resonator that leads to the maximization of the quantity  $\tau_\ell \xi_1$  or, equivalently, the minimization of  $\Delta \bar{N}_{\text{th}}$ . This height is  $h = 315$  nm, and has been found by evaluating the quantity  $\tau_\ell \xi_1$  for different values of  $h$  through FEM simulations (see Fig. S6 of the Supplemental Material [44]). Note that we have once again  $\bar{N}_{\text{tot}} \gg \Delta \bar{N}_{\text{th}}$  and thus the pumping power threshold remains practically constant with  $h$ , as we see in Fig. 4(a). As far as the second design metric is concerned,  $\xi_1$  decreases faster than  $\xi_2$  with  $h$ , leading to a reduction of the quantity  $\tau_\ell \xi_1 / \tau_\ell \xi_2$  with increasing values of  $h$ ; note that the opposite trend is obtained for increasing values of the radius  $R$ , where  $\xi_2$  decreases faster than  $\xi_1$ . This is illustrated in the inset of Fig. 4(a), where for the same  $P_p$  we get slightly higher  $P_{\text{out}}$  as  $h$  decreases, i.e., as the mode-TMD interaction is enhanced (see also Sec. S3 of the Supplemental Material [44]).

The previous discussion revealed that the choice of  $h$  has a minor impact on the cavity characteristics. However, the absorption coefficient  $\eta_p$  is significantly affected by  $h$  due to the Fabry-Perot cavity formed by the high-index SRN slab [see the inset of Fig. 4(b)]. Thus, one can minimize the required pump power by maximizing the absorption of the pump wave from the TMD, i.e., by choosing  $h$  so that the electric field inside the vertical Fabry-Perot cavity is maximum on the TMD surface (the approach to calculate  $\eta_p$  and a more complete picture of its dependence on  $h$  are included in Sec. S4 of the Supplemental Material [44]). As revealed from Fig. 4(b), the choice of  $h$  has a significant effect on the required pump power and might result in an almost fourfold decrease. The optimum height is  $h = 330$  nm, leading to both lower pumping-power threshold ( $P_{p,\text{th}} \simeq 1.3$  mW, corresponding to an intensity of 16 kW/cm<sup>2</sup>) and higher output power. As expected from the previous discussion,  $h = 330$  nm  $\simeq 3\lambda_p / (2n_{\text{SRN}})$ , a condition that maximizes the electric field on the TMD surface, thus also maximizing the absorption of the pump wave by the WSe<sub>2</sub>. It is important to note that  $\eta_p$  is maximized for every value of  $h$  that fulfills the condition  $h = m\lambda_p / (2n_{\text{SRN}})$ , where  $m$  is an integer (see Sec. S4 of the Supplemental Material [44]). However, the choice of  $h$  should be reasonable in order to maintain adequately strong interaction between the TMD bilayer and the lasing mode, on the one hand (not too thick), and reasonable radiation losses, on the other hand (not too thin). We also observe that for  $h = 250$  nm and  $h = 360$  nm the value of  $\eta_p$  is significantly lower, since now the electric field on the TMD is close to a minimum [see Fig. S7(b) of the Supplemental Material [44]].

Overall, by appropriately choosing  $h$ , one can maximize  $\eta_p$ , which, as it turns out, is the parameter that mainly influences the quantitative metrics (maximum output power and lower lasing threshold) of the proposed laser cavity. Consequently, it should be carefully chosen to optimize the lasing performance. As a final remark, we note that the calculated pumping-power thresholds are in good

agreement with reported experimental results of laser configurations based on TMD bilayers [22,23].

It is also important to discuss the thermal stability of the proposed lasing element, since its operation has been examined for a broad range of pump power densities ( $I_p = P_p/S_g$ ), spanning from a few kW/cm<sup>2</sup> to 10 MW/cm<sup>2</sup> (see Figs. 3 and 4). We have taken care that the highest considered value of  $I_p = 10$  MW/cm<sup>2</sup> is below the optical damage threshold of TMD monolayers [54]. Optical-pumping-induced heating effects could potentially alter the photoluminescence properties of the gain medium (MoS<sub>2</sub>/WSe<sub>2</sub>), by increasing its lattice temperature, and undermine the lasing operation [14,20,21]. However, the photoluminescence characteristics of TMD bilayer heterostructures have been found to be stable for pump power densities up to a few hundreds of kW/cm<sup>2</sup>

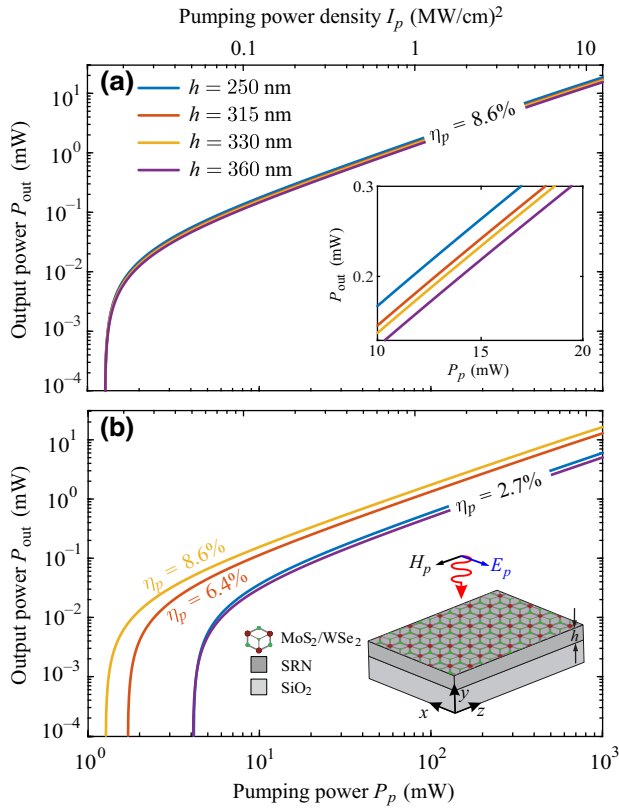


FIG. 4. Output power  $P_{\text{out}}$  as a function of the pumping power  $P_p$  (or power density  $I_p = P_p/S_g$ ) for the whispering-gallery mode of order  $m = 16$  when the height of the disk resonator is set at four different values. (a) The absorption efficiency of WSe<sub>2</sub> is artificially fixed to its maximum value of  $\eta_p = 8.6\%$ ; then  $\Delta\bar{N}_{\text{th}}$  is minimized for  $h = 315$  nm. Inset: Enlarged view of the curves above the lasing threshold to better illustrate that the second design metric improves when  $h$  is decreased. (b) The absorption efficiency  $\eta_p$  is modified with  $h$  due to the Fabry-Perot cavity formed when the lasing structure is vertically illuminated. Inset: 3D schematic of the simplified geometry used to evaluate  $\eta_p$  as  $h$  is tuned.

[20,21], i.e., an order of magnitude greater than our lasing threshold (a few tens of kW/cm<sup>2</sup>). Thus, the proposed laser can operate stably for such pumping power densities and reach practically useful output powers of 1 mW.

For these pump power densities, we have also examined the overall thermal stability of the lasing element through heat-transfer simulations with COMSOL Multiphysics® [55], by assuming that all of the power absorbed by the 2D gain medium is converted into heat (worst-case scenario). Note that SRN is practically transparent at the pump wavelength and does not act as an additional heat source. We have found that for CW pumping with powers up to 35 mW, the temperature increase does not exceed 100 K. The temperature increase will result in a shift of the resonant frequency due to the thermo-optic effect. Adopting  $\Delta T = 100$  K and the thermo-optic coefficient of SRN (comparable to that of silicon), we find a resonant frequency shift [56] in the order of 5 nm, i.e., well within the emission linewidth  $\Gamma_m$  (cf. design directive set in Sec. III). Thus, for such temperature variations, lasing operation would not be significantly obstructed. The heat removal from the

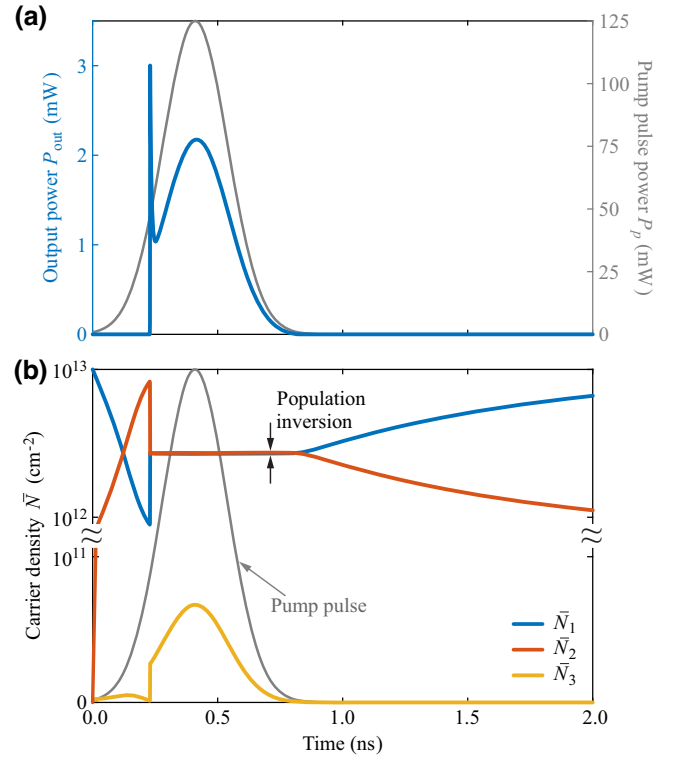


FIG. 5. Dynamic response of the proposed disk laser cavity under pulsed pump illumination. (a) Input pump pulse and the respective emitted output power. (b) Carrier-density evolution in the pump pulse time scale (ns). As the pumping pulse arrives and after population inversion is achieved, the cavity starts to emit light. When the pump fades, emission ceases and the carriers slowly return to their ground state. The radius of the disk resonator is  $R = 1.317$   $\mu\text{m}$  and the height is  $h = 330$   $\mu\text{m}$ .

lasing structure could be significantly enhanced by replacing the  $\text{SiO}_2$  cladding with a material exhibiting a similar refractive index but greater thermal conductivity, such as  $\text{MgF}_2$ , for instance, which can exhibit up to 20 times greater thermal conductivity. This results in a threefold decrease of  $\Delta T$  for the same level of pump power. In this case, CW operation with pump powers up to  $P_p = 100$  mW is possible before reaching the barrier of  $\Delta T = 100$  K. Operating with pump power levels exceeding 100 mW is still possible by exploiting pulsed pumping, i.e., using long-duration pulses (tens of nanoseconds or more) during which the lasing element operates practically CW, but the temperature increase is restricted due to the intrinsically slow thermal diffusion process [55].

Having completed the design of the cavity, and to get a more complete physical picture of the cavity emission, we examine its response under pulsed pump illumination. To excite the carriers on the TMD heterostructure, we use a Gaussian pulse with full width at half-maximum equal to 300 ps and a peak power of 125 mW. Note that, despite the high peak power of the pump pulse, its short duration results in a negligible temperature increase below 1 K, as we have calculated through heat-transfer simulations. The emitted power from the laser cavity is plotted in Fig. 5(a). We also plot the time evolution of the carrier density in each of the three energy levels of our model [Fig. 5(b)]. The arrival of the input pump pulse transfers electrons from the ground (level 1; valence band of  $\text{WSe}_2$ ) to the upper state (level 3; conduction band of  $\text{WSe}_2$ ) where electrons nonradiatively and almost instantaneously (compared

to the input pulse time scale) relax to the metastable emission level (level 2; conduction band of  $\text{MoS}_2$ ). When sufficient carriers are accumulated in level 2 and population inversion is achieved, the laser starts to emit light with an abrupt peak in  $P_{\text{out}}$ , which relaxes fast and then the emitted power follows the shape of the pumping pulse.

Furthermore, we note that the output power also follows the CW predictions of Fig. 4(b). For as much as the laser emits, the carrier populations in levels 1 and 2 remain practically constant. As the pumping pulse fades, emission ceases and the carriers slowly relax to the ground energy state. Although carrier generation through the absorption of pump photons is an almost instantaneous process, lasing does not start immediately after  $\Delta \bar{N} > \Delta \bar{N}_{\text{th}}$  [see Fig. 5(b)]. The thresholds of Eqs. (23) and (26) are CW metrics of the laser and, in pulsed pump operation, do not strictly apply due to the more complex dynamics of the cavity. Thus, although  $\tau_\ell \simeq 10$  ps (i.e., the cavity responds in a short time scale), the shorter possible pump pulse to obtain lasing is much wider, in the hundreds of picoseconds, and requires a higher peak power than the respective CW threshold. Such a complex dynamic response cannot be accurately captured by the CW metrics. Note that pulsed pump operation is typically an approach followed to get low-repetition-rate pulses; faster operation in the gigahertz scale would require external modulation schemes [8].

The TMD bilayer emits in a wide spectral range ( $\Gamma_m = 20$  Trad/s). Therefore, as a final step of the analysis of the cavity, it is interesting to examine all the modes that are supported by the disk resonator in the aforementioned

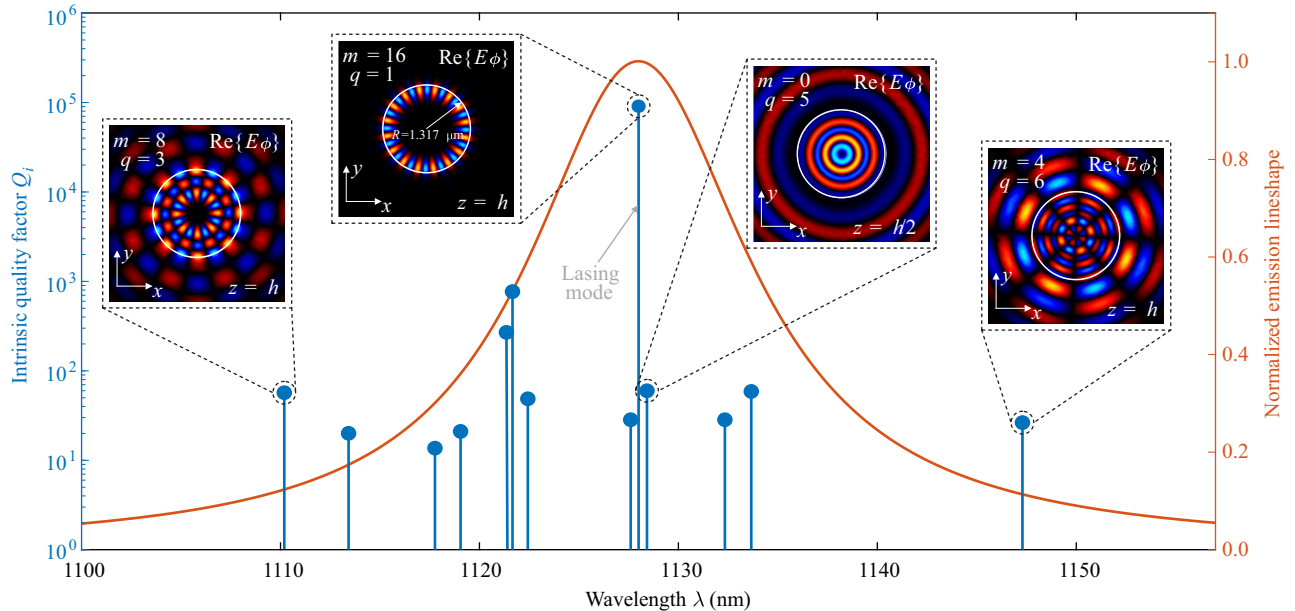


FIG. 6. Resonant frequencies and intrinsic quality factors of the supported modes in the spectral range that the TMD bilayer emits. Insets:  $\text{Re}\{E_\phi\}$  component of four characteristic modes with azimuthal order  $m$  and radial order  $q$  (including the lasing whispering-gallery mode) at either the TMD plane ( $z = h$ ) or the middle plane of the disk resonator ( $z = h/2$ ), as noted. The radius of the disk resonator is  $R = 1.317 \mu\text{m}$  and the height is  $h = 330 \mu\text{m}$ .

spectral range and discuss the likelihood of having multimode lasing in our proposed cavity. To this end, we look for all the resonant modes in the frequency range  $[\omega_m - 3\Gamma_m/2, \omega_m + 3\Gamma_m/2]$ , which covers the Lorentzian of the emission down to 10% of its maximum.

In Fig. 6 we plot the intrinsic quality factors versus the resonant wavelengths of these modes along with the normalized Lorentzian emission of the TMD bilayer. The frequency response of each cavity mode is also of Lorentzian lineshape but, for better visual representation, these lineshapes are not included. Apart from the lasing whispering-gallery mode ( $m = 16$ ), the rest of the supported modes are of higher radial order, thus characterized by low (below 1000)  $Q_i$  values (see Table S2 of the Supplemental Material [44]). This is also obvious from the insets of Fig. 6, where  $\text{Re}\{E_\phi\}$  at either the TMD plane ( $z = h$ ) or the middle plane of the resonator ( $z = h/2$ ) is depicted for a few characteristic modes. As we can see from the depicted field distributions, the modes of higher radial order are not well confined inside the cavity and exhibit strong radiation leakage. This is true for the rest of the modes, the field profile of which is not included here due to space limitations (see instead Fig. S8 of the Supplemental Material [44]).

The neighboring whispering-gallery modes of the first radial order are located at 1177 nm ( $m = 15$  order mode) and at 1083 nm ( $m = 17$  order mode), well outside the emission Lorentzian. Thus, inside the photoluminescence spectral range of the TMD bilayer, only a single first-radial-order whispering-gallery mode is supported; it is the only mode with  $Q_i$  in the order of  $10^5$ , two orders of magnitude higher than the next mode with the second-largest  $Q_i$ . Consequently, by taking into account (i) the low quality factors of the higher-radial-order modes, (ii) the spectral detuning of their resonance frequencies from  $\omega_m$ , and (iii) the spatial hole-burning effect induced by the lasing mode [the spatial depletion of the population inversion  $\Delta N(\mathbf{r}, t)$  due to the amplification of the lasing mode] [36,57,58], we can rather safely assume that we have single-mode operation in our proposed lasing structure. Finally, we note that spontaneously emitted photons are coupled to any of the supported modes with equal probability, thus cavity-induced modification (either enhancement or inhibition) of the spontaneous emission is further suppressed.

## V. CONCLUSION

To recapitulate, we have presented a framework based on perturbation theory and temporal coupled-mode theory, capable of theoretically assessing the lasing process in integrated micro- and nanophotonic cavities. The proposed version of the framework is capable of handling both bulk and contemporary sheet-type gain materials, like TMDs. The gain process is described by an induced polarization field, following a homogeneously broadened

Lorentzian oscillator, and it is rigorously introduced in the CMT framework through first-order perturbation theory. The carrier dynamics are considered through rate equations that are incorporated in the developed framework, allowing for the modeling of the most general case of “class C” lasers [59].

During the process of developing the framework, general design directives and CW metrics naturally emerged. These metrics and directives were applied for the thorough analysis and design of a practical laser cavity based on a SRNOI whispering-gallery disk resonator with a WSe<sub>2</sub>/MoS<sub>2</sub> heterostructure residing on top of the disk, acting as the gain medium. The geometric characteristics of the disk resonator (radius  $R$  and height  $h$ ) were meticulously engineered to optimize lasing performance. The interaction of the TMD bilayer both with the supported cavity modes and with the incident pump wave was considered for the optimization. The optimum parameters are summarized in Table I, alongside the obtained lasing thresholds. Importantly, the proposed framework can capture the dynamic response of the system. Finally, the supported modes in the luminescence lineshape of the TMD bilayer have been evaluated and the likelihood of multimode lasing has been discussed.

Overall, the developed CMT framework enables the accurate evaluation of fundamental laser characteristics, including the lasing threshold, the lasing frequency, and the output power, without resorting to the computationally intensive solution of the coupled Maxwell-Bloch equations. Furthermore, our theoretical framework can be expanded to accommodate gain materials with more complex behavior acquiring more energy levels, other absorption and emission processes, or even carrier diffusion and nonlinearities. The proposed laser cavity is characterized by a low pumping lasing threshold and it is capable of emitting power on the milliwatts order *inside* an integrated waveguide, with an estimated total quantum efficiency of approximately 1.7%. Hence, it can be exploited as an SOI-compatible, monolithically integrated optical source in the lower limit of the O band.

TABLE I. Optimum geometrical dimensions of the proposed laser structure. The obtained threshold population inversion  $\Delta\bar{N}_{\text{th}}$ , threshold pumping power  $P_{p,\text{th}}$ , output power  $P_{\text{out}}$  for  $P_p = 2P_{p,\text{th}}$ , and total quantum efficiency are also included.

$R$	1.317 $\mu\text{m}$
$h$	330 nm
$g$	300 nm
$\Delta\bar{N}_{\text{th}}$	$4.61 \times 10^{10} \text{ cm}^{-2}$
$P_{p,\text{th}}$	1.3 mW <sup>a</sup>
$P_{\text{out}}@2P_{p,\text{th}}$	24 $\mu\text{W}$
Total quantum efficiency	1.7%

<sup>a</sup>  $P_{p,\text{th}}$  corresponds to an input intensity of 16 kW/cm<sup>2</sup>.

## ACKNOWLEDGMENTS

The research work was supported by the Hellenic Foundation for Research and Innovation (HFRI) under the “First Call for HFRI Research Projects to support Faculty members and Researchers and the procurement of high-cost research equipment grant” (Project No. HFRI-FM17-2086).

- 
- [1] S. Liu and A. Khope, Latest advances in high-performance light sources and optical amplifiers on silicon, *J. Semicond.* **42**, 041307 (2021).
- [2] D.-S. Liu, J. Wu, H. Xu, and Z. Wang, Emerging light-emitting materials for photonic integration, *Adv. Mater.* **33**, 2003733 (2021).
- [3] A. Liu, C. Bi, R. Guo, M. Zhang, X. Qu, and J. Tian, Electroluminescence principle and performance improvement of metal halide perovskite light-emitting diodes, *Adv. Opt. Mater.* **9**, 2002167 (2021).
- [4] D. J. Blumenthal, R. Heideman, D. Geuzebroek, A. Leinse, and C. Roeloffzen, Silicon nitride in silicon photonics, *Proc. IEEE* **106**, 2209 (2018).
- [5] D. T. H. Tan, K. J. A. Ooi, and D. K. T. Ng, Nonlinear optics on silicon-rich nitride – a high nonlinear figure of merit CMOS platform [Invited], *Photonics Res.* **6**, B50 (2018).
- [6] J. You, Y. Luo, J. Yang, J. Zhang, K. Yin, K. Wei, X. Zheng, and T. Jiang, Hybrid/integrated silicon photonics Based on 2D materials in optical communication nanosystems, *Laser Photonics Rev.* **14**, 2000239 (2020).
- [7] G. Sinatkas, T. Christopoulos, O. Tsilipakos, and E. E. Kriezis, Comparative Study of Silicon Photonic Modulators Based on Transparent Conducting Oxide and Graphene, *Phys. Rev. Appl.* **12**, 064023 (2019).
- [8] G. Sinatkas, T. Christopoulos, O. Tsilipakos, and E. E. Kriezis, Electro-optic modulation in integrated photonics, *J. Appl. Phys.* **130**, 010901 (2021).
- [9] H. Tang, S. G. Menabde, T. Anwar, J. Kim, M. S. Jang, and G. Tagliabue, Photo-modulated optical and electrical properties of graphene, *Nanophotonics* **11**, 917 (2022).
- [10] C. Gies and A. Steinhoff, Atomically thin van der Waals semiconductors – a theoretical perspective, *Laser Photonics Rev.* **15**, 2000482 (2021).
- [11] Y. Li, J. Zhang, D. Huang, H. Sun, F. Fan, J. Feng, Z. Wang, and C. Z. Ning, Room-temperature continuous-wave lasing from monolayer molybdenum ditelluride integrated with a silicon nanobeam cavity, *Nat. Nanotechnol.* **12**, 987 (2017).
- [12] S. Wu, S. Buckley, J. R. Schaibley, L. Feng, J. Yan, D. G. Mandrus, F. Hatami, W. Yao, J. Vučković, A. Majumdar, and X. Xu, Monolayer semiconductor nanocavity lasers with ultralow thresholds, *Nature* **520**, 69 (2015).
- [13] Y. Ye, Z. J. Wong, X. Lu, X. Ni, H. Zhu, X. Chen, Y. Wang, and X. Zhang, Monolayer excitonic laser, *Nat. Photonics* **9**, 733 (2015).
- [14] O. Karni, E. Barré, S. C. Lau, R. Gillen, E. Y. Ma, B. Kim, K. Watanabe, T. Taniguchi, J. Maultzsch, K. Barmak, R. H. Page, and T. F. Heinz, Infrared Interlayer Exciton Emission in MoS<sub>2</sub>/WSe<sub>2</sub> Heterostructures, *Phys. Rev. Lett.* **123**, 247402 (2019).
- [15] C. Jin, E. Y. Ma, O. Karni, E. C. Regan, F. Wang, and T. F. Heinz, Ultrafast dynamics in van der Waals heterostructures, *Nat. Nanotechnol.* **13**, 994 (2018).
- [16] P. Rivera, H. Yu, K. L. Seyler, N. P. Wilson, W. Yao, and X. Xu, Interlayer valley excitons in heterobilayers of transition metal dichalcogenides, *Nat. Nanotechnol.* **13**, 1004 (2018).
- [17] H. Fang, C. Battaglia, C. Carraro, S. Nemsak, B. Ozdol, J. S. Kang, H. A. Bechtel, S. B. Desai, F. Kronast, A. A. Unal, G. Conti, C. Conlon, G. K. Palsson, M. C. Martin, A. M. Minor, C. S. Fadley, E. Yablonovitch, R. Maboudian, and A. Javey, Strong interlayer coupling in van der Waals heterostructures built from single-layer chalcogenides, *Proc. Natl. Acad. Sci. U.S.A.* **111**, 6198 (2014).
- [18] F. Ceballos, M. Z. Bellus, H. Y. Chiu, and H. Zhao, Probing charge transfer excitons in a MoSe<sub>2</sub>-WS<sub>2</sub> van der Waals heterostructure, *Nanoscale* **7**, 17523 (2015).
- [19] H. Zhu, J. Wang, Z. Gong, Y. D. Kim, J. Hone, and X. Y. Zhu, Interfacial charge transfer circumventing momentum mismatch at two-dimensional van der Waals heterojunctions, *Nano Lett.* **17**, 3591 (2017).
- [20] B. Miller, A. Steinhoff, B. Pano, J. Klein, F. Jahnke, A. Holleitner, and U. Wurstbauer, Long-lived direct and indirect interlayer excitons in van der Waals heterostructures, *Nano Lett.* **17**, 5229 (2017).
- [21] P. Nagler, G. Plechinger, M. V. Ballottin, A. Mitioglu, S. Meier, N. Paradiso, C. Strunk, A. Chernikov, P. C. Christianen, C. Schüller, and T. Korn, Interlayer exciton dynamics in a dichalcogenide monolayer heterostructure, *2D Materials* **4**, 025112 (2017).
- [22] E. Y. Paik, L. Zhang, G. W. Burg, R. Gogna, E. Tutuc, and H. Deng, Interlayer exciton laser of extended spatial coherence in atomically thin heterostructures, *Nature* **576**, 80 (2019).
- [23] Y. Liu, H. Fang, A. Rasmita, Y. Zhou, J. Li, T. Yu, Q. Xiong, N. Zheludev, J. Liu, and W. Gao, Room temperature nanocavity laser with interlayer excitons in 2D heterostructures, *Sci. Adv.* **5**, eaav4506 (2019).
- [24] R. M. Ma and R. F. Oulton, Applications of nanolasers, *Nat. Nanotechnol.* **14**, 12 (2019).
- [25] T. Wang, D. K. Ng, S. K. Ng, Y. T. Toh, A. K. Chee, G. F. Chen, Q. Wang, and D. T. Tan, Supercontinuum generation in bandgap engineered, back-end CMOS compatible silicon rich nitride waveguides, *Laser Photonics Rev.* **9**, 498 (2015).
- [26] M. Lamy, C. Finot, A. Parriaux, C. Lacava, T. D. Bucio, F. Gardes, G. Millot, P. Petropoulos, and K. Hammani, Si-rich Si nitride waveguides for optical transmissions and toward wavelength conversion around 2 μm, *Appl. Opt.* **58**, 5165 (2019).
- [27] M. R. Karim, N. A. Kayed, M. R. Hossain, and B. M. A. Rahman, Study of low-peak-power highly coherent broadband supercontinuum generation through a dispersion-engineered Si-rich silicon nitride waveguide, *Appl. Opt.* **59**, 5948 (2020).
- [28] Y. Cao, B. U. Sohn, H. Gao, P. Xing, G. F. Chen, D. K. Ng, and D. T. Tan, Supercontinuum generation in a nonlinear ultra-silicon-rich nitride waveguide, *Sci. Rep.* **12**, 1 (2022).
- [29] H. A. Haus, *Waves and Fields in Optoelectronics* (Prentice-Hall, Engelwood Cliffs, NJ, 1984), 1st ed.

- [30] S. Fan, W. Suh, and J. D. Joannopoulos, Temporal coupled-mode theory for the Fano resonance in optical resonators, *J. Opt. Soc. Am. A* **20**, 569 (2003).
- [31] W. Suh, Z. Wang, and S. Fan, Temporal coupled-mode theory and the presence of non-orthogonal modes in lossless multimode cavities, *IEEE J. Quantum Electron.* **40**, 1511 (2004).
- [32] T. Christopoulos, O. Tsilipakos, N. Grivas, and E. E. Kriezis, Coupled-mode-theory framework for nonlinear resonators comprising graphene, *Phys. Rev. E* **94**, 062219 (2016).
- [33] V. G. Ataloglou, T. Christopoulos, and E. E. Kriezis, Nonlinear coupled-mode-theory framework for graphene-induced saturable absorption in nanophotonic resonant structures, *Phys. Rev. A* **97**, 063836 (2018).
- [34] T. Christopoulos, O. Tsilipakos, G. Sinatkas, and E. E. Kriezis, Degenerate four-wave mixing in nonlinear resonators comprising two-dimensional materials: A coupled-mode theory approach, *Phys. Rev. B* **98**, 235421 (2018).
- [35] S.-L. Chua, Y. Chong, A. D. Stone, M. Soljacic, and J. Bravo-Abad, Low-threshold lasing action in photonic crystal slabs enabled by Fano resonances, *Opt. Express* **19**, 1539 (2011).
- [36] A. E. Siegman, *Lasers* (University Science Books, Sausalito, CA, 1986).
- [37] J. Bravo-Abad, S. Fan, S. G. Johnson, J. D. Joannopoulos, and M. Soljacic, Modeling nonlinear optical phenomena in nanophotonics, *J. Lightwave Technol.* **25**, 2539 (2007).
- [38] M. Chitsazi, S. Factor, J. Schindler, H. Ramezani, F. M. Ellis, and T. Kottos, Experimental observation of lasing shutdown via asymmetric gain, *Phys. Rev. A* **89**, 043842 (2014).
- [39] J. Shena, J. Hizanidis, N. E. Kouvaris, and G. P. Tsironis, Localized patterns in star networks of class-B lasers with optoelectronic feedback, *Phys. Rev. A* **98**, 053817 (2018).
- [40] Y. Kominis, A. Bountis, and V. Kovanis, Radically tunable ultrafast photonic oscillators via differential pumping, *J. Appl. Phys.* **127**, 083103 (2020).
- [41] S. Droulias, S. Mohamed, H. Rekola, T. K. Hakala, C. M. Soukoulis, and T. Koschny, Experimental demonstration of dark-state metasurface laser with controllable radiative coupling, *Adv. Opt. Mater.* **10**, 2102679 (2022).
- [42] J. D. Joannopoulos, S. G. Johnson, J. N. Winn, and R. D. Meade, *Photonic Crystals: Molding the Flow of Light* (Princeton University Press, Princeton, NJ, 2008), 2nd ed.
- [43] T. Christopoulos, O. Tsilipakos, G. Sinatkas, and E. E. Kriezis, On the calculation of the quality factor in contemporary photonic resonant structures, *Opt. Express* **27**, 14505 (2019).
- [44] See Supplemental Material at <http://link.aps.org/supplemental/10.1103/PhysRevApplied.19.064027> for supplemental comments, figures, and tables.
- [45] S.-L. Chua, B. Zhen, J. Lee, J. Bravo-Abad, O. Shapira, and M. Soljacic, Modeling of threshold and dynamics behavior of organic nanostructured lasers, *J. Mater. Chem. C* **2**, 1463 (2014).
- [46] L. Ge, Y. D. Chong, and A. D. Stone, Steady-state ab initio laser theory: Generalizations and analytic results, *Phys. Rev. A* **82**, 063824 (2010).
- [47] C. Hsu, R. Frisenda, R. Schmidt, A. Arora, S. M. de Vasconcellos, R. Bratschitsch, H. S. van der Zant, and A. Castellanos-Gomez, Thickness-dependent refractive index of 1L, 2L, and 3L MoS<sub>2</sub>, MoSe<sub>2</sub>, WS<sub>2</sub>, and WSe<sub>2</sub>, *Adv. Opt. Mater.* **7**, 1900239 (2019).
- [48] C. Javerzac-Galy, A. Kumar, R. D. Schilling, N. Piro, S. Khorasani, M. Barbone, I. Goykhman, J. B. Khurgin, A. C. Ferrari, and T. J. Kippenberg, Excitonic emission of monolayer semiconductors near-field coupled to high-*Q* microresonators, *Nano Lett.* **18**, 3138 (2018).
- [49] G. Moody, C. Kavir Dass, K. Hao, C. H. Chen, L. J. Li, A. Singh, K. Tran, G. Clark, X. Xu, G. Berghäuser, E. Malic, A. Knorr, and X. Li, Intrinsic homogeneous linewidth and broadening mechanisms of excitons in monolayer transition metal dichalcogenides, *Nat. Commun.* **6**, 8315 (2015).
- [50] Y. Yu, Y. Yu, L. Huang, H. Peng, L. Xiong, and L. Cao, Giant gating tunability of optical refractive index in transition metal dichalcogenide monolayers, *Nano Lett.* **17**, 3613 (2017).
- [51] T. Christopoulos, O. Tsilipakos, and E. E. Kriezis, Perturbation theory for Kerr nonlinear leaky cavities, *Opt. Lett.* **45**, 6442 (2020).
- [52] H. L. Liu, C. C. Shen, S. H. Su, C. L. Hsu, M. Y. Li, and L. J. Li, Optical properties of monolayer transition metal dichalcogenides probed by spectroscopic ellipsometry, *Appl. Phys. Lett.* **105**, 201905 (2014).
- [53] G. Nousios, T. Christopoulos, O. Tsilipakos, and E. E. Kriezis, Dynamic routing through saturable absorption in graphene photonic resonators: Impact of carrier diffusion and finite relaxation time, *J. Appl. Phys.* **131**, 053104 (2022).
- [54] A. Castellanos-Gomez, M. Barkelid, A. M. Goossens, V. E. Calado, H. S. Van Der Zant, and G. A. Steele, Laser-thinning of MoS<sub>2</sub>: On demand generation of a single-layer semiconductor, *Nano Lett.* **12**, 3187 (2012).
- [55] O. Tsilipakos, T. V. Yioultsis, and E. E. Kriezis, Theoretical analysis of thermally tunable microring resonator filters made of dielectric-loaded plasmonic waveguides, *J. Appl. Phys.* **106**, 093109 (2009).
- [56] N. G. Pruiti, C. Klitis, C. Gough, S. May, and M. Sorel, Thermo-optic coefficient of PECVD silicon-rich silicon nitride, *Opt. Lett.* **45**, 6242 (2020).
- [57] K. Schuhmann, K. Kirch, F. Nez, R. Pohl, G. Wichmann, and A. Antognini, Spatial hole burning in thin-disk lasers and twisted-mode operation, *Appl. Opt.* **57**, 2900 (2018).
- [58] C. Wang, F. HadavandMirzaee, and T.-H. Her, Universal Output Characteristics of Single-Mode Operation in Low-Loss Large-*V*-Number Multimode Waveguide Lasers with Transverse Spatial Hole Burning, *Phys. Rev. Appl.* **13**, 024042 (2020).
- [59] L. Narducci and N. Abraham, *Laser Physics and Laser Instabilities* (World Scientific, Singapore, 1988).